UNIVERSITY OF CALIFORNIA
RIVERSIDE

Quantum Transport Properties of Atomically Thin Black Phosphorus

A Dissertation submitted in partial satisfaction
of the requirements for the degree of

Doctor of Philosophy

in

Physics

by

Nathaniel Alan Gillgren

June 2017

Dissertation Committee:
Dr. Chun Ning (Jeanie) Lau
Dr. Shan-Wen Tsai
Dr. Nathan Gabor

The Dissertation of Nathaniel Alan Gillgren is approved:

_____

_____

_____

Committee Chairperson

University of California, Riverside

Acknowledgement

Firstly, I would like to thank my advisor Professor Jeanie Lau. She has always provided me with the motivation and support I needed to pursue my research interests. I feel incredibly indebted to her for her advice and mentorship. Her guidance on both experiments and manuscript preparation has proven invaluable in my growth as a scientist and I am inspired by her intellect and depth of knowledge.

Besides my advisor I would like to thank my qualifying exam and thesis committee: Professor Marc Bockrath, Professor Shan-wen Tsai, Professor Nathan Gabor and Professor Jianlin Liu for their insightful discussion and encouraging discussions.

My sincerest thanks go to my collaborators who were instrumental in both experimental and theoretical results. Jin Hu, Jiang Wei, Xue Liu and Zhiqiang Mao provided the first black phosphorus samples where we observed quantum oscillations. Yafis Barlas, Dasharna Wickramartane, and Roger K. Lake performed the theoretical calculations for comparison to our experimental results. Takashi Taniguchi and Kenji Watanabe grew the high quality boron nitride crystal structures which we used to stabilize black phosphorus.

I would like to share my deep gratitude towards all my lab mates: Yongjin Lee, Fenglin Wang, Jhao-Wun Huang, Kevin Myrho, Yanmeng Shi, Petr Stepanov, Son Tran, Jiawei Yang, Yulu Liu and Dmitry Scherbakov. I am incredibly indebted to Yongjin Lee and Kevin Myrho who taught me the fundamentals of semiconductor fabrication and Fenling Wang and Jhao-Wun who laid the ground work for heterostructure assembly. Despite never collaborating on published work I consider Petr Stepanov my “comrade in

arms" as our friendly rivalry during the development of our labs' edge contact recipes was one of the most memorable periods during my tenure. I am forever grateful to Yanmeng Shi whose collaboration on weak localization measurements was instrumental in the publication of our results. Finally I would like to thank Jiawei Yang and Son Tran who have taken up where I left off in black phosphorus research. I hope nothing but the best for all my lab mates.

Chapter 4, chapter 5, and figure 1.1 are re-used with permission from 2D materials (chapter 1 Ref. 48, and 49). They were published as, "Gate tunable quantum oscillations in air-stable and high mobility few-layer phosphorene heterostructures", and "Weak localization and electron–electron interactions in few layer black phosphorus devices". Figure 1.2 (chapter 1 Ref. 50) is re-used with permission from PNAS with the title, "The Renaissance of Black Phosphorus".

Finally I would like to thank my family: my parents, my brother and my wife for all their emotional support and encouragement.

ABSTRACT OF THE DISSERTATION

Quantum Transport Properties of Atomically Thin Black Phosphorus

by

Nathaniel Alan Gillgren

Doctor of Philosophy, Graduate Program in Physics
University of California, Riverside, June 2017
Dr. Chun Ning (Jeanie) Lau, Chairperson

Since the discovery of graphene, two-dimensional (2D) van der Waals materials research has flourished, with new crystals and novel phenomena discovered at a rapid pace. In 2014, black phosphorus (BP) was rediscovered as a member of 2D materials, displaying high quality electronic transport with in-plane anisotropy, though the first generation of layered devices suffered from poor stability and relatively low mobility. In this thesis, we overcome these challenges by employing van der Waals assembly techniques to create BP devices sandwiched between thin hexagonal boron nitride layers. These devices are air-stable, for more than two weeks, and boast mobility up to 500 $cm^2V^{-1}s^{-1}$ at room temperature and 4,000 $cm^2V^{-1}s^{-1}$ at low temperature. Using two-point and four-point geometries with global and local gates, we observe Shubnikov de Haas oscillations that yield effective mass of holes ~0.25 m_e to 0.31 m_e, where m_e is the mass of the electron. From weak localization measurements, we obtain phase relaxation length of ~30 nm to 100 nm. Moreover, we determine mobility bottleneck and transport mechanism from temperature dependence measurements: when the device is highly hole

doped, the mobility μ exhibits power law dependence on temperature T, $\mu \sim T^{0.6,}$ suggesting that it is limited by charged impurity scattering; close to the band edge, conduction is dominated by variable range hopping, with estimated localization length ~ 1.7 nm – 30 nm. The studies presented here contributed to our understanding of electronic properties of atomically thin BP, and will help to guide future efforts in fabrication, exploring, and engineering devices based on 2D semiconductors.

Table of Contents

List of Figures

Chapter 1

Introduction

1.1 Introduction

Since the discovery of graphene in 2004[1], two-dimensional (2D) materials have emerged as one of the most active frontiers of condensed matter research. The layered structure of 2D materials allow easy isolation by the so-called "scotch tape method" of mechanical exfoliation, thus affording researchers easy access to the interesting physical properties of 2D materials without the need for highly specialized growth chambers. The research of 2D materials research began with graphene[1,2] and has since branched out to include other materials, including but not limited to hexagonal boron nitride[3] (BN), transition metal dichalcogenides[4,5] (TMD) and black phosphorus (BP).

1.2 Graphene and Transition Metal Dichalcogenides

Graphene possesses some of the most unique physics in the 2D materials research community and is still under intense study to date. One of the first discoveries in graphene was the anomalous "half-integer" quantum Hall Effect in monolayer graphene that manifests in quantum hall plateau sequence (in units of e^2/h) of $(N+1/2)$, instead of N in traditional semiconductors (here N is an integer).[2,6] In addition, monolayer and few-layer graphene host unusual energy-momentum dispersions. For instance, in single, bi- and ABC-stacked tri-layer graphene, the energy scales as p^N, where N is the number of layers.[7,8] In the single layer case, the massless dispersion relationship is similar to that of photons with a reduced "speed of light", $c \sim 1\text{x}10^6$ m/s. This massless, relativistic dispersion has many intriguing consequences, such as the Klein paradox (perfect

tunneling of relativistic particles across high and wide potential barriers).[9,10] Moreover, the presence of an electronic state at zero energy in graphene provides a great platform for investigating electronic interactions, e.g. a spontaneous gap opening near the neutrality point in bilayer graphene and rhombohedral trilayer graphene[11–14], and a quantum Hall state at filling factor 0 that has no counterpart in GaAs-based semiconductors.[15–17]

In contrast to graphene's small or non-existent bad gaps, TMD's possess large band gaps that lead to interesting optoelectronic and electronic physics. When TMD's are exfoliated down to the single layer, they transition from an indirect band gap semiconductor to a direct gap semiconductor, which significantly increases light emission and photoluminescence quantum yield.[18,19] In addition, the large binding energies between electron hole pairs that arise from the reduced screening from the confinement in two dimensions lead to interesting excitonic physics. Furthermore, the valley configuration of an exciton where the electron and hole are in the same valley but have opposing spins directly correspond to the circular polarization of the emitted/absorbed photon.[20] In addition to these exciting optoelectronic phenomena, recent experiments demonstrated Ising superconductivity in layered MoS_2, where electron spins are pinned to out-of-plane directions and strongly enhance the in-plane upper critical field that exceeds the paramagnetic limit.[21–23]

Despite the rich physics afforded by graphene and TMD, there is a significant gap in the device properties between graphene and TMD, as illustrated in figure 1.2. The size of band gap is relatively small or non-existent in graphene, while it ranges from 1 – 2 eV

in TMDs. This leaves an unexplored territory for devices with band gaps between 0.1 – 1 eV. There is also a gap in mobility between graphene (10^4 to 10^6 $cm^2V^{-1}s^{-1}$) and TMD (~100 $cm^2V^{-1}s^{-1}$ in most devices, though progress has been made in fabricating high quality devices[24]). These gaps are now bridged by the emergence of yet another 2D material – atomically thin black phosphorus.

1.3 Bulk Black phosphorus

Bulk Black phosphorus was first synthesized by Bridgeman in 1914 by conversion of white phosphorus at 200 ^{0}C and 1.2 GPa[25]. It is the only stable allotrope of phosphorus. Unlike white phosphorus' body-centered cubic structure, BP has a layered-orthorhombic lattice. Early electrical measurements on bulk BP demonstrated p-type doping at low temperatures, phonon limited mobilities up to 3000 $cm^2V^{-1}s^1$, and a band gap of 0.33eV.[26]

Due to its puckered structure, BP exhibits strong anisotropic properties. Electrical measurements on high quality samples with mobilities up to 60,000 $cm^2V^{-1}s^1$ showed that the mobility differs by a factor of 3 between the two in-plane (*x* and *y*) directions and differs by almost one order of magnitude between the in-plane and out-of-plane directions.[27] Typical undoped devices demonstrated *p*-type conduction while *n*-type conduction was achieved by Te impurities.[27] Far-infrared measurements reported large anisotropies of the effective mass in both *p*- and *n*-doped samples with the largest difference occurring between the armchair (0.648 m_e) and zig-zag (0.0761 m_e) directions.[28] Additional anisotropies were observed along the in-plane axis via

synchrotron radiation measurements with observations of excitons between the 2p and 2s modes.[29]

BP is highly sensitive to pressure, demonstrating both electrical and crystallographic transitions. Neutron powder diffraction experiments demonstrated anisotropic compression with the shortening of van der Waals bonds between layers and a shearing motion within the layers.[30] Reversible crystollographic transitions from orthorhombic to rhombohedral and finally to simple cubic were observed around 5GPa, and 10GPa respectively.[31] The resistivity exhibits a strong dependence on pressure that varies from 2 x 10^{-2} Ωcm at atmospheric pressure to 1 x 10^{-5} Ω*cm at 15GPa.[32] Sharp drops in the resistivity at 5 GPa and 10 GPa correlate strongly with the crystallographic transitions and temperature measurements between these transitions revealed a semiconductor to semi-metal to metal electronic transition.[32] Additionally, with increasing pressure, the band gap is reduced and eventually closed at 4-5 GPa, consistent with the electronic transition between semiconductor to semimetal.[32] It is interesting to note that the gap does not close in a linear fashion: at around 2 GPa, a kink occurs along the gap *vs* pressure diagram which indicates an electronic transition not associated with a crystallographic transition.[32]

Pressure experiments also revealed the presence of superconductivity in the simple-cubic phase, typically above the transition pressure of 10 GPa.[33] The observed critical temperatures T_c are pressure dependent with values ranging from 6 K at 10 GPa to 12K at 30 GPa.[33,34] Furthermore, T_c is strongly dependent on the temperature-pressure path. When BP is cooled in the rhombohedral and simple cubic phase from 300K to 4K,

T_c is weakly pressure dependent. However, when BP is cooled from the orthorhombic phase, T_c displays a strong pressure dependence, strongly suggesting that the semiconducting phase plays an important role.[34] This is further corroborated by x-ray diffraction profiles which show the presence of the orthorhombic phase as high 8 GPa when the sample is cooled down in the semiconducting phase before the application of large pressures.[34]

1.4 Layered Black Phosphorus

The properties of bulk BP clearly demonstrate attractive qualities such as strong anisotropic properties, rich pressure-dependent electrical and crystallographic phases, and anomalous superconducting states. These early experiments, coupled with the rapid rise of graphene and TMDs, motivated several groups to explore this fascinating material in its layered form. The first wave of studies reported the isolation and electrical characterization of thin BP devices that had mobilities ranging from 200 – 1000 $cm^2V^{-1}s^{-1}$, drain current modulation ranging from 10^3 – 10^5, and ambipolar transport[35–37]. Device mobility was found to be thickness dependent with the highest mobility of 1000 $cm^2V^{-1}s^{-1}$ observed at 10nm-thick samples[35]. By using a circular array of contacts, the in-plane and angle-dependent conductivity was observed with an anisotropic ratio of around 1.5[36]. A similar ratio of 1.66 was observed in a dual 90 degree dual hall bar device[38]. These results are in stark contrast to the anisotropy ratio of the in-plane effective mass ratio of 8.5 observed in bulk crystals [28].

Theoretical and experimental studies into the optical response of layered BP also revealed a number of interesting properties. Optical measurements discovered long

thermal decay lengths up to 1 μm and broadband photo-response to excitation wavelengths from 400 – 940 nm along with a fast 1ms rise time[39–41]. An excitionic structure is deduced from anisotropic dispersive modes, and theoretical calculations suggest a strong excitonic structure with an in-plane electric field that would enable the investigation of the stark effect in high ionizing fields.[42,43] Lastly, theoretical calculations predicted a layer dependent band-gap, with the single layer predicted to have a gap of 2eV.[44]

Despite the rapid progress of the electrical and optical characterization of layered BP, it still suffers from low mobility compared to that of the bulk. Another problem is its rapid degradation[45–47] in ambient conditions. Although BP is the most stable form of phosphorus, when exfoliated into thin layers, it becomes highly reactive and degrades electronically and physically in air within days. Using atomic force microscopy (AFM) and electrical measurements, Island *et al* observed layer by layer etching of BP flakes in ambient conditions and identified physisorbed oxygen and nitrogen, and water absorption as the main culprits for device breakdown[46]. Favron *et al* used Raman and TEM studies and reported on the thickness dependent photoassisted oxidation reaction with oxygen dissolved in water[47]. Such instability posed a significant challenge in fabrication of stable, high quality devices.

In the following chapters, I will describe our research on fabrication and transport measurements of high mobility, air stable BP devices. Chapter 2 will briefly discuss several phenomena that are prototypical of quantum transport in low dimensions: Shubnikov de Hass oscillations, weak localization and variable range hopping. I will

describe in detail the various fabrication processes and techniques I used to make devices in Chapter 3, including the encapsulation and passivation of BP using BN. In chapter 4, 5 and 6, I report the results of our research, which includes one of the first observations of quantum oscillations in BP, a record high mobility of 4000 $cm^2V^{-1}s^{-1}$, density dependent effective mass and phase relaxation lengths, and gate tunable average hopping lengths[48,49]. Finally, in chapter 7, I will discuss the current status and future prospect of BP research.

References

1. Novoselov, K. S. *et al.* Electric field effect in atomically thin carbon films. *Science (80-.).* **306,** 666–669 (2004).

2. Zhang, Y., Tan, Y.-W., Stormer, H. L. & Kim, P. Experimental observation of the quantum Hall effect and Berry's phase in graphene. *Nature* **438,** 201–204 (2005).

3. R., D. *et al.* Boron nitride substrates for high-quality graphene electronics. *Nat Nano* **5,** 722–726 (2010).

4. Ganatra, R. & Zhang, Q. Few-Layer MoS2: A Promising Layered Semiconductor. *ACS Nano* **8,** 4074–4099 (2014).

5. Chhowalla, M. *et al.* The chemistry of two-dimensional layered transition metal dichalcogenide nanosheets. *Nat Chem* **5,** 263–275 (2013).

6. Novoselov, K. S. *et al.* Two-dimensional gas of massless Dirac fermions in graphene. *Nature* **438,** 197–200 (2005).

7. McCann, E., Abergel, D. S. L. & Fal'ko, V. I. The low energy electronic band structure of bilayer graphene. *Eur. Phys. J. Spec. Top.* **148,** 91–103 (2007).

8. Zhang, F., Sahu, B., Min, H. & MacDonald, A. H. Band structure of A B C -stacked graphene trilayers. *Phys. Rev. B* **82,** 35409 (2010).

9. Katsnelson, M. I., Novoselov, K. S. & Geim, A. K. Chiral tunnelling and the Klein paradox in graphene. *Nat. Phys.* **2,** 620–625 (2006).

10. Young, A. F. & Kim, P. Quantum interference and Klein tunnelling in graphene heterojunctions. *Nat. Phys.* **5,** 222–226 (2009).

11. VelascoJ. *et al.* Transport spectroscopy of symmetry-broken insulating states in bilayer graphene. *Nat Nano* **7,** 156–160 (2012).

12. Bao, W. *et al.* Stacking-dependent band gap and quantum transport in trilayer graphene. *Nat. Phys.* **7,** 948–952 (2011).

13. Weitz, R. T., Allen, M. T., Feldman, B. E., Martin, J. & Yacoby, A. Graphene Broken-Symmetry States in Doubly Gated Suspended Bilayer Broken-Symmetry States in Doubly Gated Suspended Bilayer Graphene. **812,** (2010).

14. Freitag, F., Trbovic, J., Weiss, M. & Schonenberger, C. Spontaneously Gapped Ground State in Suspended Bilayer Graphene. *Phys. Rev. Lett.* **108,** 76602 (2012).

15. Checkelsky, J. G., Li, L. & Ong, N. P. Zero-Energy State in Graphene in a High

Magnetic Field. *Phys. Rev. Lett.* **100,** 206801 (2008).

16. Kharitonov, M. Phase diagram for the ν = 0 quantum Hall state in monolayer graphene. *Phys. Rev. B* **85,** 155439 (2012).

17. Zhao, Y., Cadden-Zimansky, P., Jiang, Z. & Kim, P. Symmetry Breaking in the Zero-Energy Landau Level in Bilayer Graphene. doi:10.1103/PhysRevLett.104.066801

18. Yeh, P.-C. *et al.* Layer-dependent electronic structure of an atomically heavy two-dimensional dichalcogenide. *Phys. Rev. B* **91,** 41407 (2015).

19. Lezama, I. G. *et al.* Indirect-to-Direct Band Gap Crossover in Few-Layer MoTe2. *Nano Lett.* **15,** 2336–2342 (2015).

20. Yu, H., Cui, X., Xu, X. & Yao, W. Valley excitons in two-dimensional semiconductors. *Natl. Sci. Rev.* **2,** 57–70 (2015).

21. Shi, W. *et al.* Superconductivity Series in Transition Metal Dichalcogenides by Ionic Gating. *Sci. Rep.* **5,** 12534 (2015).

22. Costanzo, D., Jo, S., Berger, H. & Morpurgo, A. F. Gate-induced superconductivity in atomically thin MoS2 crystals. *Nat Nano* **11,** 339–344 (2016).

23. Zhou, B. T., Yuan, N. F. Q., Jiang, H.-L. & Law, K. T. Ising superconductivity and Majorana fermions in transition-metal dichalcogenides. *Phys. Rev. B* **93,** 180501 (2016).

24. Cui, X. *et al.* Multi-terminal transport measurements of MoS2 using a van der Waals heterostructure device platform. *Nat Nano* **10,** 534–540 (2015).

25. Bridgman, P. W. TWO NEW MODIFICATIONS OF PHOSPHORUS. *J. Am. Chem. Soc.* **36,** 1344–1363 (1914).

26. Keyes, R. W. The Electrical Properties of Black Phosphorus. *Phys. Rev.* **92,** 580–584 (1953).

27. Akahama, Y., Endo, S. & Narita, S. Electrical Properties of Black Phosphorus Single Crystals. *Journal of the Physical Society of Japan* **52,** 2148–2155 (1983).

28. Narita, S. *et al.* Far-Infrared Cyclotron Resonance Absorptions in Black Phosphorus Single Crystals. *J. Phys. Soc. Japan* **52,** 3544–3553 (1983).

29. Taniguchi, M. *et al.* Core-level reflectance spectroscopy of black phosphorus single crystals. *Phys. Rev. B* **28,** 1165–1167 (1983).

30. Cartz, L., Srinivasa, S. R., Riedner, R. J., Jorgensen, J. D. & Worlton, T. G. Effect of pressure on bonding in black phosphorus. *J. Chem. Phys.* **71,** 1718–1721 (1979).

31. Jamieson, J. C. Crystal Structures Adopted by Black Phosphorus at High Pressures. *Science (80-.).* **139,** (1963).

32. Okajima, M., Endo, S., Akahama, Y. & Narita, S. Electrical Investigation of Phase Transition in Black Phosphorus under High Pressure. *Jpn. J. Appl. Phys.* **23,** 15–19 (1984).

33. Kawamura, H., Shirotani, I. & Tachikawa, K. Anomalous superconductivity in black phosphorus under high pressures. *Solid State Commun.* **49,** 879–881 (1984).

34. Kawamura, H., Shirotani, I. & Tachikawa, K. Anomalous superconductivity and pressure induced phase transitions in black phosphorus. *Solid State Commun.* **54,** 775–778 (1985).

35. Li, L. *et al.* Black phosphorus field-effect transistors. *Nat. Nanotechnol.* **9,** 372–377 (2014).

36. Liu, H. *et al.* Phosphorene: An Unexplored 2D Semiconductor with a High Hole Mobility. *ACS Nano* **8,** 4033–4041 (2014).

37. Koenig, S. P., Doganov, R. A., Schmidt, H., Castro Neto, A. H. & Özyilmaz, B. Electric field effect in ultrathin black phosphorus. *Appl. Phys. Lett.* **104,** 103106 (2014).

38. Mishchenko, A. *et al.* Nonlocal Response and Anamorphosis: The Case of Few-Layer Black Phosphorus. *Nano Lett.* **15,** 6991–6995 (2015).

39. Low, T., Engel, M., Steiner, M. & Avouris, P. Origin of photoresponse in black phosphorus phototransistors. *Phys. Rev. B* **90,** 81408 (2014).

40. Buscema, M. *et al.* Fast and Broadband Photoresponse of Few-Layer Black Phosphorus Field-Effect Transistors. *Nano Lett.* **14,** 3347–3352 (2014).

41. Buscema, M., Groenendijk, D. J., Steele, G. A., van der Zant, H. S. J. & Castellanos-Gomez, A. Photovoltaic effect in few-layer black phosphorus PN junctions defined by local electrostatic gating. *Nat. Commun.* **5,** 4651 (2014).

42. Schuster, R., Trinckauf, J., Habenicht, C., Knupfer, M. & Büchner, B. Anisotropic Particle-Hole Excitations in Black Phosphorus. *Phys. Rev. Lett.* **115,** 26404 (2015).

43. Chaves, A., Low, T., Avouris, P., Çakır, D. & Peeters, F. M. Anisotropic exciton Stark shift in black phosphorus. *Phys. Rev. B* **91,** 155311 (2015).

44. Tran, V., Soklaski, R., Liang, Y. & Yang, L. Layer-controlled band gap and anisotropic excitons in few-layer black phosphorus. *Phys. Rev. B* **89,** 235319 (2014).

45. Castellanos-Gomez, A. *et al.* Isolation and characterization of few-layer black phosphorus. *2D Mater.* **1,** 25001 (2014).

46. Island, J. O., Steele, G. A., Zant, H. S. J. van der & Castellanos-Gomez, A. Environmental instability of few-layer black phosphorus. *2D Mater.* **2,** 11002 (2015).

47. Favron, A. *et al.* Photooxidation and quantum confinement effects in exfoliated black phosphorus. *Nat Mater* **14,** 826–832 (2015).

48. Gillgren, N. *et al.* Gate tunable quantum oscillations in air-stable and high mobility few-layer phosphorene heterostructures. *2D Mater.* **2,** 11001 (2014).

49. Shi, Y. *et al.* Weak localization and electron–electron interactions in few layer black phosphorus devices. *2D Mater.* **3,** 34003 (2016).

50. Ling, X., Wang, H., Huang, S., Xia, F. & Dresselhaus, M. S. The renaissance of black phosphorus. *Proc. Natl. Acad. Sci.* **112,** 201416581 (2015).

Fig. 1.1. (a) Crystal structure of black phosphorus layers. From the top view one can see the striking resemblance to the honeycomb lattice of graphene. This is immediately lost in the side view which shows the puckered nature of BP layers. Re-used with permission from ref 48)

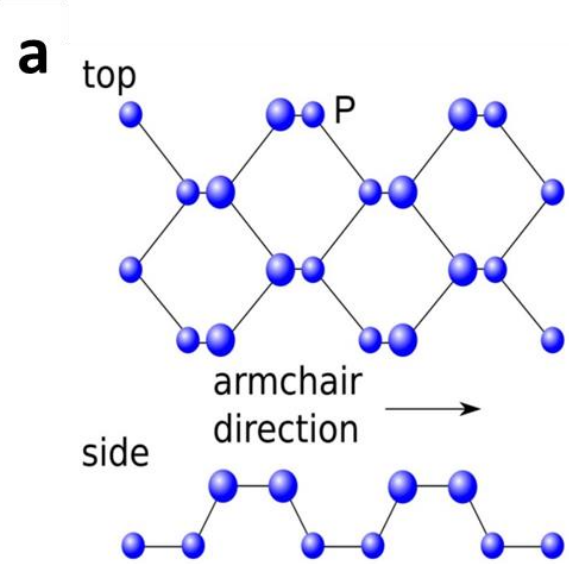

Fig. 1.2. (a) The mobility/on-off ratio of graphene, BP and TMD's. Areas indicated for graphene (black squares and grey shaded circle), layered BP (purple dots and light purple shaded circle) and TMDs (green dots and light green shaded circle). The dots correspond to data from specific references (numbers refer to the citation index from the review which this graph was adapted from). (b) Band gap ranges for graphene, BP and TMD's. Re-used with permission from 50.

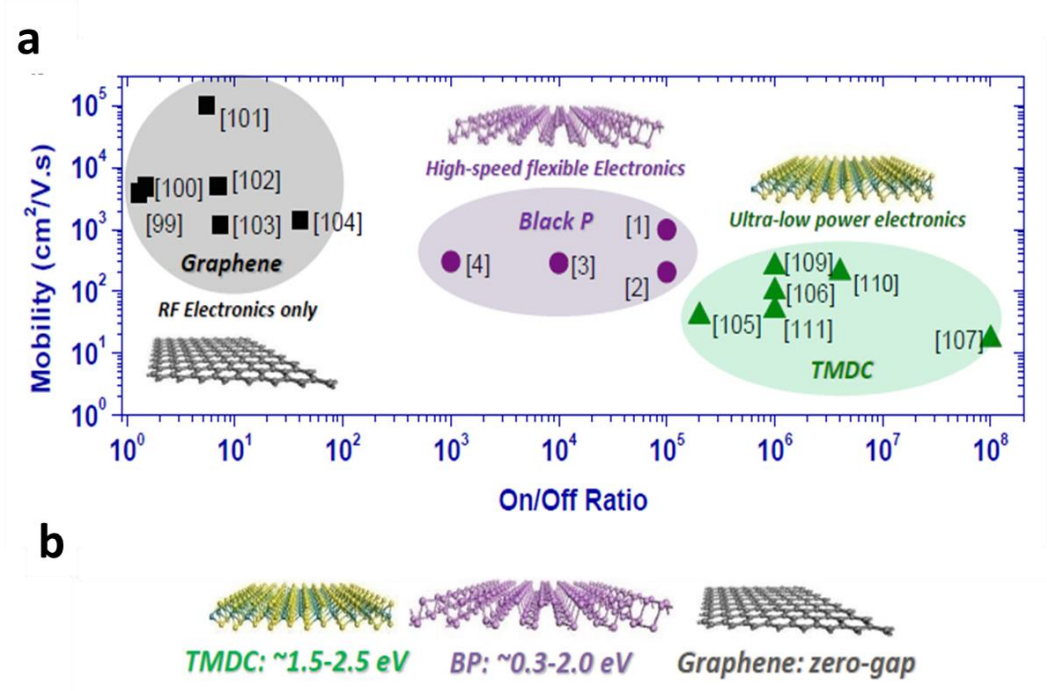

Chapter 2

Background

2.1 Introduction

In this chapter, I will discuss the various transport phenomena in 2D electronic systems, including the mechanisms of Shubnikov de Haas oscillations (SdHO), weak localization and variable range hopping. I will provide a theoretical background on these topics and highlight the relevant models and equations.

2.2 Shubnikov de Haas oscillations

Classically, when charge carriers propagate with a velocity perpendicular to a magnetic field they undergo cyclotron motion, with frequency given by $\omega_c = eB/m$, where e is the electron charge, B the magnetic field, and m the mass of the electron. Quantum mechanically, the particle's motion in a sufficiently strong vector potential leads to the quantum harmonic oscillator solution with discrete energy eigenstates, called Landau levels. These Landau levels (Fig. 2.1a) have energies $E_n = \hbar\omega_c(n + ½)$, where n is a positive integer. The magnetic field directly controls the size of the energy separation through ω_c, as well as the degeneracy of each state through the relation $D = (2S+1)\ \Phi/\Phi_o$, where S is the spin of the system, $\Phi = BA$ is the flux through the device, and $\Phi_o = h/e$ is the flux quanta. In electronic systems $S = ½$ and the above relation reduces to $D = 2\ \Phi/\Phi_o$. If the magnetic field strength is comparable to the Zeeman energy $\mu_B B$, where μ_B is the Bohr magneton, then the spin degeneracy is lifted and the occupation level becomes $D = \Phi/\Phi_o$.

As the Landau levels are separated by an energy gap, $\hbar\omega_c$, when the Fermi energy is between successive levels, the longitudinal resistance R goes to zero (Fig. 2.1a), while the Hall resistance R_H is quantized in units of e^2/h. This is the celebrated quantum Hall effect. In real systems, disorder due to impurity scattering and thermal broadening affect the system (Fig 2.2a). To observe the quantum hall effect the momentum relaxation time must be smaller than the cyclotron period, and this leads to the relation $\mu > B^{-1}$ (see chapter 3 for derivation). Thus the effects of Landau levels are expected to be observable around 1T if the mobility is 10,000 $cm^2\ V^{-1}\ S^{-1}$. In SdHO, R never goes to zero and R_H is typically not quantized, which is due to incomplete confinement in the third dimension that provides additional scattering states, so that the density of states between Landau levels is not truly zero. Nevertheless these states are still observable in the oscillatory behavior of the conductivity.

These oscillations can be experimentally tuned by two different parameters. Traditionally one modulates B, which in turn increases the Landau level spacing $\hbar\omega_c$ and degeneracy of each LL. Thus as B increases, successive Landau levels "rise" in energy and move pass the Fermi level that stays constant. Alternatively, oscillations can also be tuned by changing carrier density in two dimensional systems. In this case, as the density is increased the Fermi level "rises" between Landau levels where B remains constant and the spacing is constant.

SdHO are quantitatively described by the Lifshitz-Kosevich formula. [1,2]

$$\frac{\Delta R_{xx}}{R_{xx}} \propto \frac{\lambda}{\sinh\lambda} e^{-\lambda_D} \cos\left\{\frac{2\pi E_f}{\hbar\omega} + \pi\right\} \qquad (1)$$

Here $\lambda = \frac{2\pi^2 k_B T}{\hbar \omega_c}$, $\omega_c = eB/m^*$ is the cyclotron frequency, m^* the cyclotron mass of charge carriers, k_B the Boltzmann's constant, E_F the Fermi level and $\lambda_D = \frac{2\pi^2 k_B T_D}{\hbar \omega_c}$. T_D is the Dingle temperature, given by $k_B T_D = \frac{\hbar}{2\pi\tau}$, where τ is the transport lifetime. SdHO have been used extensively to map the Fermi surface of transport carriers and determine carrier concentrations.

2.3 Weak Localization

Weak localization occurs in confined samples at cryogenic temperatures. It is a negative quantum correction to the classical conductivity, arising from the enhanced backscattering from time reversed paths of phase coherent carrier wave amplitudes. The following treatment is borrowed from Datta.[3]

In a phase coherent region of a conductor the probability $R(m \rightarrow n)$ that an incident electron in mode m will be reflected into mode n is obtained by squaring the sum of the amplitude for all possible paths connecting m to n. $R(m \rightarrow n) = |A_1(m \rightarrow n) + A_2(m \rightarrow n) + \ldots|^2$ Here the individual path is a particular sequence of scattering events from m to n as shown in figure 2.

$$A(m \rightarrow n) = t(m \rightarrow m_1) r(m_1 \rightarrow m_2) t(m_2 \rightarrow n) \exp[i(k_m L_m + k_{m1} L_{m1} + k_{m2} L_{m2} + k_n L_n)]$$

where L_m is the length between each scattering event with wavevector k_m. Usually the phases are random so that the square of the sum equals to the sum of the squares. However, the phases are not random in the case when the initial and final states are the same, $m = n$. In this case there exists a time reversal path A_R for each A which leads to $R(m \rightarrow m) = |A + A_R|^2$. If the region is phase coherent and there is no magnetic field then

$A_R = A$ and the sum becomes $4A^2$. But if the region is not phase coherent then the sum becomes $2A^2$. Therefore coherent backscattering doubles the reflection probability when $m = n$ and the conductivity of the sample is reduced from that expected from the classical value.

In 2D, this treatment leads to a correction to the classical conductance with the following equation $\sigma_Q = \sigma_{CL} - 2e^2/h\pi\ ln(\tau_\varphi/\tau_m)$ where τ_φ is the phase relaxation time, that has characteristic temperature dependence $\sim T^{-\alpha}$, where α is 1, and τ_m is the momentum relaxation time.[1,3] It should be noted that for electron-electron interactions corrections to the conductivity also scale with $\sim ln(1/T\tau_m)$, and therefore temperature measurements alone are not sufficient to distinguish between the two phenomena. This ambiguity is easily resolved with the application of a magnetic field. By applying a perpendicular magnetic field, the time reversal symmetry of coherent back scattering carriers is broken and the conductance will increase.

Hikami, Larkin, and Nagoaka provided a quantitative equation to this problem leading to the following equation for the relative change in conductance in a magnetic field.[4]

$$\Delta\sigma = \sigma(B) - \sigma(B = 0) = -\frac{e^2}{\pi h}\left[ln\left(\frac{B_\varphi}{B}\right) - \Psi\left(\frac{1}{2} + \frac{B_\varphi}{B}\right)\right] \qquad (2)$$

Here σ is the device conductivity, h is Planck's constant, e is the electron charge, Ψ is the digamma function, $B_\varphi = \frac{\hbar}{4eL_\varphi^2}$ is the magnetic field required to destroy phase coherence, $L_\varphi = \sqrt{D\tau_\varphi}$, and D is the diffusion coefficient.

2.4 Variable Range Hopping

Variable range hopping (VRH) occurs in strongly disordered systems at low temperatures where measured activation energies are much smaller than expected for Schottky barrier emission. Instead of diffusive or ballistic transport where carriers are free to move in a gas-like fasion, carriers in variable rang hopping are confined to localized states where they have a finite probability to "hop" between these states. Depending on the strength of electronic interactions, transport may occur in Mott or Efros-Shkolovskii (EF) regimes.

When electronic interactions are negligible, transport occurs in the Mott VRH regime. The following treatment is borrowed from Hapert.[5]The probability P of a carrier to tunnel from a localized state i with energy E_i to an empty state j with energy E_j can be described by $exp(-2\alpha R_{ij} - (E_j - E_i)/k_BT)$. Here k_B is boltzman constant, T the temperature of the system, and R_{ij} the distance between state i and j. The parameter α^{-1} is the localization parameter of these states and conceptually is the relative size for a hydrogen-like localized wave function. The range $S = 2\alpha R_{ij} + (E_j - E_i)/k_BT$ is defined as the higher dimensional range which is the "distance" in both spatial and energy coordinates. The probability P then becomes $exp(-S)$. The conductivity is determined by the probability of sequential hops, and as these multiply the average is the geometric mean giving

$$\sigma \sim exp\left[\lim_{n\to\infty} \frac{1}{n}\sum_{i}^{n} \ln P_i\right] \stackrel{\text{def}}{=} \exp(-S_{nn}) \qquad (3)$$

Here S_{nn} is the average nearest neighbor hopping range.

S_{nn} can be determined in the following way. At a given temperature T the carrier will hop from one site to another within a radius $r(T)$. Statistically the average distance from the original site is $L = ¾\ r(T)$. The energy difference between the original site and this average hopping site will be $W \sim 1/D(\varepsilon)r(T)^3 \sim 1/D(\varepsilon)L^3$, where $D(\varepsilon)$ is the density of localized states. Thus the average range $S = 2\alpha L + A/D(\varepsilon)L^3 k_B T$, where A is a constant; minimizing S with respect to L yields the average hopping range $S_{nn} \sim (A/\alpha D(\varepsilon)k_B T)^{1/4}$, which can be written as $S \sim (T_o/T)^{1/4}$. The conductivity is then written as[6]

$$\sigma \sim \exp\left(-\left(\frac{T_o}{T}\right)^{\frac{1}{4}}\right) \qquad (4)$$

The above treatment is valid for three dimensional materials with small electric fields and constant density of states. In general, for d dimensions, the conductivity can be written as $\sigma \sim exp\ (T^{\nu})$, where $\nu = (d+1)^{-1}$. This treatment can be extended to cases where the electric field is non-negligible: in the 2D case, $\sigma \sim exp\ (E^{\nu})$, where E is the applied electric field, and ν is defined as above.[7]

In the above treatment electronic interactions were ignored, but if the strength of these interactions is non-negligible, then effects of the Couloumb gap on the density of states must be considered. This leads to similar behavior, $\sigma \sim exp\ (T^{\nu})$, but with $\nu = ½$ for both 3D and 2D systems. This similarly extends to the electric field behavior $\sigma \sim exp\ (E^{\nu})$, where, again, $\nu = ½$.

2.5 Conclusion

In this chapter we have provided the relevant models and equations which will be applied to the results of our measurements in BP devices. In chapter 4, we use SdHO to

extrapolate the density dependence of the effective mass of BP and compare it to tight binding calculations. In chapter 5, we use weak localization measurements to obation the phase relaxation length as a function of gate voltage and its temperature dependence. Finally, in chapter 6, we discuss the localization size of disordered states in local gated BP devices.

References

1. Ando, T., Fowler, A. B. & Stern, F. Electronic properties of two-dimensional systems. *Rev. Mod. Phys.* **54,** 437–672 (1982).

2. Coleridge, P. T., Stoner, R. & Fletcher, R. Low-field transport coefficients in GaAs/ Ga 1 − x Al x As heterostructures. *Phys. Rev. B* **39,** 1120–1124 (1989).

3. Datta, S. *Electronic Transport in Mesoscopic Systems*. (Cambridge University Press 1995, 2013).

4. Hikami, S., Larkin, A. I. & Nagaoka, Y. Spin-Orbit Interaction and Magnetoresistance in the Two Dimensional Random System. *Prog. Theor. Phys.* **63,** 707–710 (1980).

5. Hapert, J. J. van. Hopping Conduction and Chemical Structure : a study on Silicon Suboxides. (2002). at <https://dspace.library.uu.nl/handle/1874/672>

6. Mott, N. F. Conduction in non-crystalline materials. *Philos. Mag.* **19,** 835–852 (1969).

7. Singh, M., Thompson, R. B. & Dumas, O. Electric-field-dependent variable-range hopping conductance in quasi-two-dimensional systems: Application to PrBa 2 Cu 3 O 7 − y -based superconductor–normal-metal–superconductor junctions. *Phys. Rev. B* **53,** 6806–6810 (1996).

Figure 2.1. Energy eigenstates of charge carriers moving perpendicular to a magnetic field. 1a) depicts the ideal case with no disorder broadening with energy states separated by $\hbar\omega$. When the Fermi energy E_F is between successive energy levels the longitudinal resistance will go to zero as there are no accessible transport paths and it will rise to some finite value when E_F overlaps an allowed energy state. However in real samples disorder broadening 1b) creates additional energy states between eigenstates, thus preventing R from vanishing.

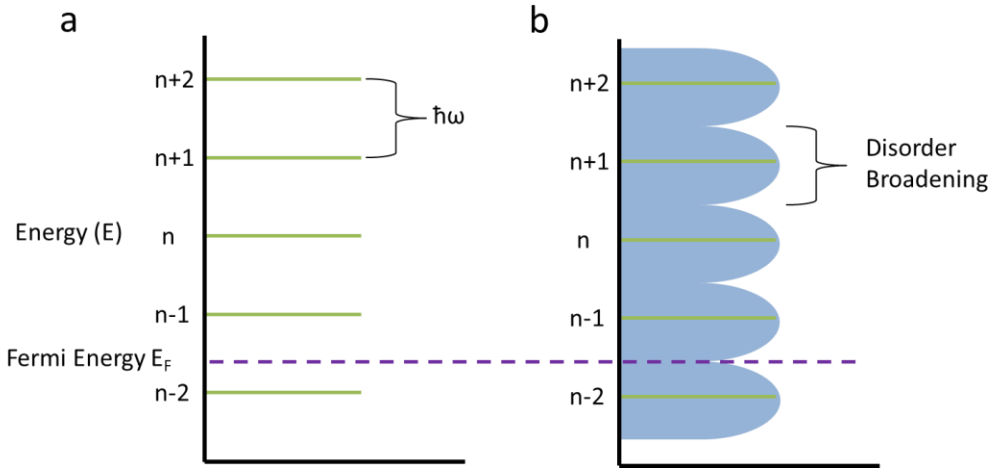

Figure 2.2. A particular sequence of scattering events of a carrier wave from $m \rightarrow n$. Each event can be modeled by transmission or reflection amplitude $t(m \rightarrow m_1)$.

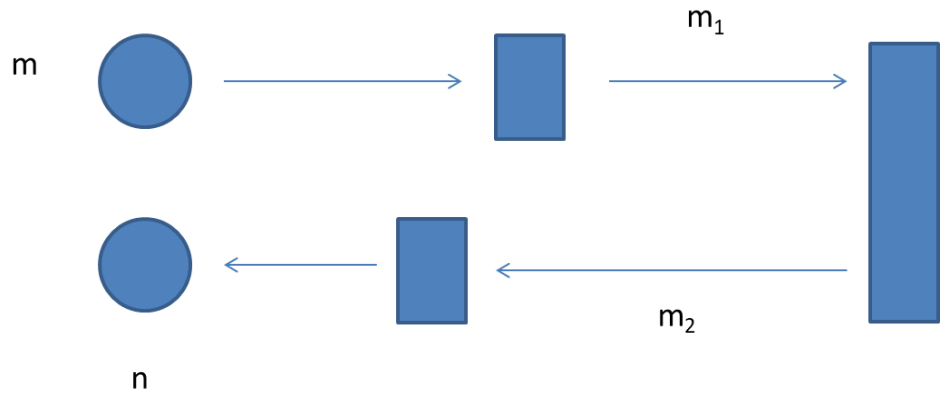

Chapter 3

Fabrication

3.1 Introduction

The fabrication of high quality devices is crucial to the observation of quantum phenomena described in this thesis. One of the most widely used metrics for device quality is mobility, which is a macroscopic measurement directly tied to the microscopic parameter – momentum relaxation time τ_m, defined by the relation $\mu = e\,\tau_m / m^*$, where e is the electron charge, and m^* is the effective mass. The higher the mobility, the larger the relaxation time, and thus fewer scattering centers. While "high" mobility is a relative concept and depends on the material under investigation, in this thesis high mobility samples will typically refer to those in which quantum phenomena can be observed in our laboratory. For instance, in order to observe SdHO, a carrier must be able to complete at least one period of cyclotron motion in a magnetic field B before it is scattered as the cyclotron period τ_c is given by m^*/eB, the requirement of $\tau_c < \tau_m$ leads to $\mu >\sim B^{-1}$, as the condition for observing SdHO. In other words, to observe SdHO at or below 1 T, the device should have mobility exceeding 10,000 $cm^2V^{-1}s^{-1}$.

As discussed in chapter 1, the first generation of BP devices suffered from limited mobility and poor stability. Achieving high mobility necessitates minimization of both intrinsic and extrinsic scatterers, such as defects, impurities, phonons, corrugation, etc. Defects and impurities in the lattice are largely determined during crystal synthesis. Most bulk BP crystals used for research presented in this thesis are synthesized by low pressure catalytic chemical vapor transport with AuSn and SnI_4 powder[1,2], and provided to us by

Smart Elements or Dr. Zhiqiang Mao's group at Tulane University. More recently, we also experimented with BP crystals grown by a high-pressure high-temperature technique from Dr. Takahashi Taniguchi's group at National institute for Materials Science, which consistently yielded devices with higher mobility, suggesting fewer defects/impurities in the bulk crystal.

This chapter focuses primarily on the fabrication and minimization of extrinsic defects. All our devices are fabricated on silicon substrates with 300 nm of silicon oxide. In general, this substrate is atomically coarse on the atomic scale and prone to trapped charges, and is often the limiting factor in device quality. For instance, by simply removing the substrate by hydrofluoric acid, graphene devices with ultra-high mobility exceeding 450,000 $cm^2V^{-1}s^{-1}$ have been demonstrated.[5–10] However, these suspended devices are very fragile and prone to electrical and mechanical instabilities. An alternative route to mobility engineering is to use a different substrate. Hexagonal boron nitride (hBN) emerged as a high quality layered substrate, as it is atomically flat, free of dangling-bonds and compatible with most device geometries.[11]

The following sections will provide detailed descriptions of the fabrication process and techniques I used to create high quality devices. Section 3.2 describes the mechanical exfoliation of layered samples from bulk crystals, section 3.3 discusses the construction of hetero-structures consisting of BP encapsulated between BN, and section 3.4 describes the fabrication of electrical contacts via plasma etching.

3.2 Mechanical Exfoliation

To prepare samples of either BN or BP, we employed the so called “scotch tape” method. Bulk crystals were cut into suitable sized pieces with a razor blade and placed in the center of tape parallel to the long edge and roughly a third of the distance from the short edge (Fig. 3.1a). The tape was then folded over and layers of the bulk crystal were peeled away. The tape is first folded over at roughly a 45 degree angle and peeled away (Fig. 3.1.b - 3.1.c), then folded at the same angle taking extra care not to overlap the peeled crystal flakes. In order to preserve the quality and optimize the size of thin layers, the peeling of the tape was repeated in such a way as to minimize overlap from successive peelings of the crystal layers. This creates a line as shown in Fig. 3.1.d of exfoliated crystals. The angle of exfoliation is changed by 90 degrees (Fig. 3.1.e) and the peeling is repeated until a third of the tape is filled (Fig. 3.1.f). Finally the rest of the tape is covered with the crystal demonstrated in figure. 3.1.g.

Once the tape is prepared, the samples are then deposited onto SiO_2 or Polydimethylsiloxane (PDMS). An optical microscope is used to identify suitable flakes for fabrication and measurement. The deposition technique is very similar between SiO_2 and PDMS. In general, the tape is placed onto the substrate and then peeled away leaving thin layered flakes. For SiO_2, the peeling rate is slow to moderate, while for PDMS the peeling rate is done in a quick jerk-like motion, much like waxing legs. I found that slower peeling rates on PDMS resulted in fewer flakes or none at all. Various pieces of BP and BN are shown in figure 3.2 on both SiO_2 and PDMS.

3.3 Transfer Stages

To fabricate encapsulated heterostructures, two atomic layers randomly placed on two different substrates must be aligned and brought into contact under an optical microscope, and transfer one of the layers by releasing from its substrate. The first generation of transfer microscope was assembled from an inspection microscope and a an XY stage attached to a focusing rack.[1,12] This provided control of both X, Y, and Z direction of two surfaces while monitoring through the microscope lens. The major drawbacks of this stage were the lack of rotational and tilt control that result in poor alignment and low yield. The second generation of transfer stages lead by Petr Stepanov directly followed the parts list from Castellanos-Gomez et al.[13] This stage possesses X, Y, Z, rotation and tilt control while increasing the monitoring zoom by a factor of 2.

3.4 Stamps

PDMS stamps are the back bone of the entire assembly process. They provide a substrate to both manipulate layered crystals and are transparent enough to see through optically. The stamps are made from a glass slide and a 1cm x 1cm PDMS square placed in the middle. I used both commercial and home-made PDMS squares to varying degrees of success. The former is typically thinner, thus more optically transparent allowing easier alignment and transfer. The disadvantage is that the tilt angle between planes of the stamp and sample must be precisely aligned. I mainly used Home-made stamps, but found success with both.

Home-made PDMS squares were made by mixing a standard 10:1 ratio of PDMS and curing agent that is then placed in vacuum for 10 minutes to remove air pockets. The

PDMS was then poured into molds followed by 1-10 minute exposure at 150 Celsius to speed up the curing process. The mold was cut into suitable sized square pieces and gently placed onto clean glass slides ensuring that the two surfaces were in optimal contact. The competed stamps are used in the top-down and bottom-up assembly techniques described in sections 3.5 and 3.6.

The PDMS stamps must undergo an additional step to prepare for the top-down stacking method (see section 3.6 below) – spinning and baking a sacrificial polymer layer onto the stamp. For all top-down transfers in this thesis I used polypropylene carbonate (PPC). To prepare the PPC for spin/baking it is dissolved in anisole at a 10:1 ratio by weight and heated to 80 – 120 degrees Celsius in a fume hood. Extra care is made not to bring the solution above the boiling point of anisole, which is 150 degrees Celsius. This sacrificial layer is spin/baked onto the PDMS stamps at a rate of 8-10,000 rpm and then heated on a hot plate at 180 degrees C for 30s – 60s to evaporate the anisole. If the anisole is not removed from the PPC after spin/baking BP and BN will not adhere to the sacrificial layer and the transferring will fail.

3.5 "Bottom-up" Assembly of Heterostructures

As the name implies the bottom-up method consists of stacking the heterostructure from the bottom to the top. First BP and BN flakes are exfoliated onto PDMS stamps, and an additional BN flake is exfoliated onto SiO_2 (Fig. 3.3.a). The BP and BN on PDMS stamps are then deposited onto the BN on SiO_2. The flakes are transferred by first bringing the flake on PDMS into direct contact with the BN on SiO_2 (Fig. 3.3.b). Once in contact the stamp is slowly peeled away (Fig. 3.3.c). Due to the van

der Waals' interactions between the flakes, they remain in contact while the PDMS is removed. This is process is repeated (Fig. 3.3.d) until the BN-BP-BN hetero-structure is formed (Fig. 3.3.e). This method is quick and efficient – the assembly takes between 30 – 90 minutes and the process is solvent free. Its biggest drawback is polymer residue left by the PDMS on the atomic layers.

3.6 "Top-down" Assembly of Heterostructures

The top-down method consists of stacking the hetero-structure from the top to the bottom. Here BN and BP are prepared on SiO_2 substrates (Fig. 3.4.a). The PPC/PDMS stamp is then brought into contact with the top BN flake (Fig. 3.4.b). Once in contact, the temperature of the stage is brought to 35-50 degrees Celsius which is above the glass transition temperature of PPC. This step increases adhesion between BN and PPC. Once at elevated temperatures, the PPC/PDMS stamp is quickly lifted, peeling both the stamp and BN from the SiO_2 (Fig. 3.4.c). Next, the BN/PPC/PDMS is aligned and brought into contact with the BP flake (Fig. 3.4.d). The previous steps of heating and peeling are repeated until the BN/BP/BN structure is assembled on the PPC/PDMS stamp (Fig. 3.4.e). In the last step, the stack is released onto a SiO_2 chip by heating the stage above 90 °C (Fig. 3.4.f). Above 90 $^{\circ}$C, PPC releases itself from PDMS, leaving the BN/BP/BN stack on the surface along with the PPC layer. The chip is immersed in chloroform for 10 minutes to dissolve the PPC layer, rinsed with IPA and then dried with nitrogen gas.

3.7 Contact Fabrication

Once the heterostructures are complete, contacts are fabricated using electron (e-) beam lithography, plasma etching and e-beam evaporation. While the top layer of BN

protects BP from degradation, it unfortunately also prevents the direct fabrication of electrical contacts. To achieve contact, we used ICP etching to expose the BP. Due to thickness variation between samples, two types of contact geometries emerged: edge contact, when the stack is completely etched and the edge is exposed for contact, and surface contact when the top layer of BN is etched so that a partially etched surface of BP is exposed for contact. Both methods work, but we find that surface contact has a higher success rate. See figure 5 for a detailed sketch of the two methods.

To prepare heterostructure samples for e-beam lithography two layers of Poly(methyl methacrylate) (PMMA) are spin/baked over the chips. The chips are spun at 4000 rpm for 60s followed by a 1-10 minute bake at 180 degree Celsius. Silver paint dissolved in IPA is placed on the chip after PMMA near the heterostructure which provides a physical feature for focusing the e-beam and creates a geographical marker for exposing the subsequent alignment marks. This alignment mark matrix, consisting of an array of squares at 60-µm intervals, is exposed using e-beam lithography, developed with 3:1 IPA:MIBK solution and metallized by evaporating 10/100nm Cr/Au, followed by liftoff in acetone. The alignment marks are also labeled at 300µm intervals by coordinate pairs (i.e. (0,0), (0,1), (2,0), etc…) with (2,2) denoting the center of the matrix. To ensure the matrix is near the hetero-structure, a small blob of silver paint is applied to the chip.

Two optical micrographs of the AM at 600x and at 100x magnification, respectively, are then uploaded to NPGS DesignCAD to design various patterns for contacts, bonding pads, etching patterns and gates. In some cases, the etching pattern and contact pattern are the same. Sample designs are shown in figure 6. Each category is

saved separately by layer and uploaded to a NPGS design file where dose parameters are set for each pattern. Dose tests are performed periodically to ensure that each pattern is properly exposed.

Once the designs are completed, PMMA is again spin/baked onto the chip and the etching pattern is written to expose the BP for metal deposition. The stack is etched with SF_6 in an ICP etcher. When making edge contact, the hetero-structure is etched for 30-40s or until the entire stack is etched. For partial etching, the hetero-structure is etched in 3-4s intervals. Between each interval, the stack is observed under a microscope to determine if the BP is properly exposed. This is done by monitoring the color contrast of the top BN. BN appears light to dark blue depending on its thickness, while the SiO_2 surface is purple. When the top layer of BN changes from blue to purple, the top BN layer is completely removed.

If the etching pattern is the same as the contact, then immediately after etching the device is put into an e-beam evaporator for metal deposition. We generally deposit 10 nm Cr and 100 nm Au for contacts, though thicknesses ranging from 5 – 15 for Cr and 100 – 200 can be used. Both Cr and Au are evaporated at a rate of 0.1 – 0.2 nm/min in high vacuum (10^{-6} torr). If the etching and contact patterns are not the same, then PMMA is removed using acetone and a new layer of PMMA is spin/baked onto the chip, followed by lithography to fabricate the contact and bonding pad patterns.

Lastly, top gates are deposited on to the BN/BP/BN heterostructure. If the top BN layer is relatively thick (> 10nm) and crack-free, then it will act as an insulator and gate dielectric. In this case, a gate pattern is written directly onto the BN above the BP and

Cr/Au is deposited. If the BN is thin (< 10nm) or shows large cracks, an additional lithography step is performed to deposit AlO by e-beam evaporation at a rate of 0.05 – 0.1 nm/min in 10^{-6} torr vacuum, followed by the fabrication of the gate and metal electrode.

3.8 Conclusion

These fabrication techniques are the foundation of high quality BP devices. Both mobility bottlenecks and poor stability are alleviated by encapsulation. The bottom BN layer provides a high quality substrate and decreases extrinsic defects which lead to higher mobility devices. The top BN provides an encapsulating layer which protects the BP from water and oxygen degradation. These methods provided the samples which ultimately lead to the first observation of SdHO in BP as well as the highest mobility achieved at time of publication. In addition, the bottom-up and top-down methods for encapsulating BP between BN can be easily extended to fabricate devices based on other 2D materials.

References

1. Gillgren, N. *et al.* Gate tunable quantum oscillations in air-stable and high mobility few-layer phosphorene heterostructures. *2D Mater.* **2,** 11001 (2014).

2. Shi, Y. *et al.* Weak localization and electron–electron interactions in few layer black phosphorus devices. *2D Mater.* **3,** 34003 (2016).

3. Shi, Y. *et al.* Weak localization and electron–electron interactions in few layer black phosphorus devices. *2D Mater.* **3,** 34003 (2016).

4. Tran, S. *et al.* Surface Transport and Quantum Hall Effect in Ambipolar Black Phosphorus Double Quantum Wells. (2017). at <http://arxiv.org/abs/1703.04911>

5. Bolotin, K. I. *et al. Ultrahigh electron mobility in suspended graphene*. *Solid State Communications* **146,** (2008).

6. VelascoJ. *et al.* Transport spectroscopy of symmetry-broken insulating states in bilayer graphene. *Nat Nano* **7,** 156–160 (2012).

7. Bao, W. *et al.* Stacking-dependent band gap and quantum transport in trilayer graphene. *Nat. Phys.* **7,** 948–952 (2011).

8. Lee, Y. *et al.* Competition between spontaneous symmetry breaking and single-particle gaps in trilayer graphene. *Nat. Commun.* **5,** 5656 (2014).

9. Lee, Y. *et al.* Multicomponent Quantum Hall Ferromagnetism and Landau Level Crossing in Rhombohedral Trilayer Graphene. *Nano Lett.* **16,** 227–31 (2016).

10. Ki, D.-K., Fal'ko, V. I., Abanin, D. A. & Morpurgo, A. F. Observation of Even Denominator Fractional Quantum Hall Effect in Suspended Bilayer Graphene. *Nano Lett.* **14,** 2135–2139 (2014).

11. R., D. *et al.* Boron nitride substrates for high-quality graphene electronics. *Nat Nano* **5,** 722–726 (2010).

12. Stepanov, P. *et al.* Tunable Symmetries of Integer and Fractional Quantum Hall Phases in Heterostructures with Multiple Dirac Bands. *Phys. Rev. Lett.* **117,** 76807 (2016).

13. Castellanos-Gomez, A. *et al.* Deterministic transfer of two-dimensional materials by all-dry viscoelastic stamping. *2D Mater.* **1,** 11002 (2014).

Figure 3.1. Schematic of exfoliation process. Handles are formed by folding tape back onto itself (a) Bulk BP is placed a third of the way from handle. (b) – (d) at a 45 degree angle the tape is folded to form a line of BP flakes. (e) – (f) The folding direction is rotated by 90 degrees, and roughly a third to half the tape is filled in. Extra care is taken to ensure no overlap between each folding process, so that each exfoliated surface is as clean as possible. (g) The rest of the tape is filled in and the tape is then ready for exfoliation onto the desired substrate.

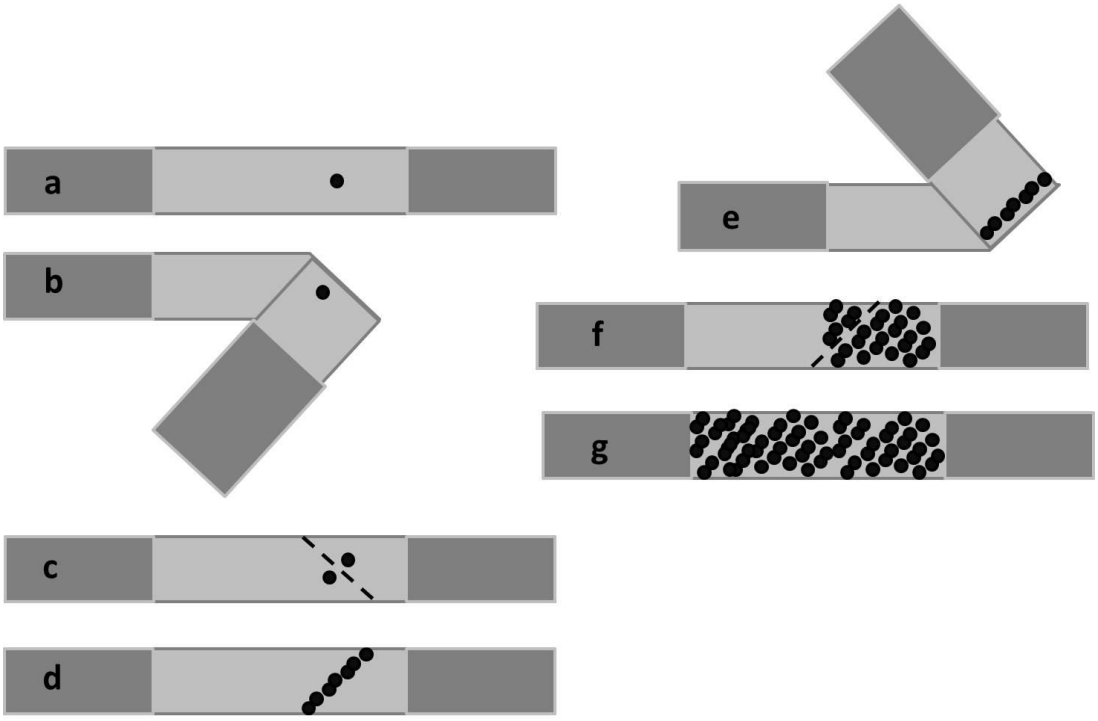

Figure 3.2. BP flakes on PDMS stamps and SiO_2 substrates. Scale bar is 30μm

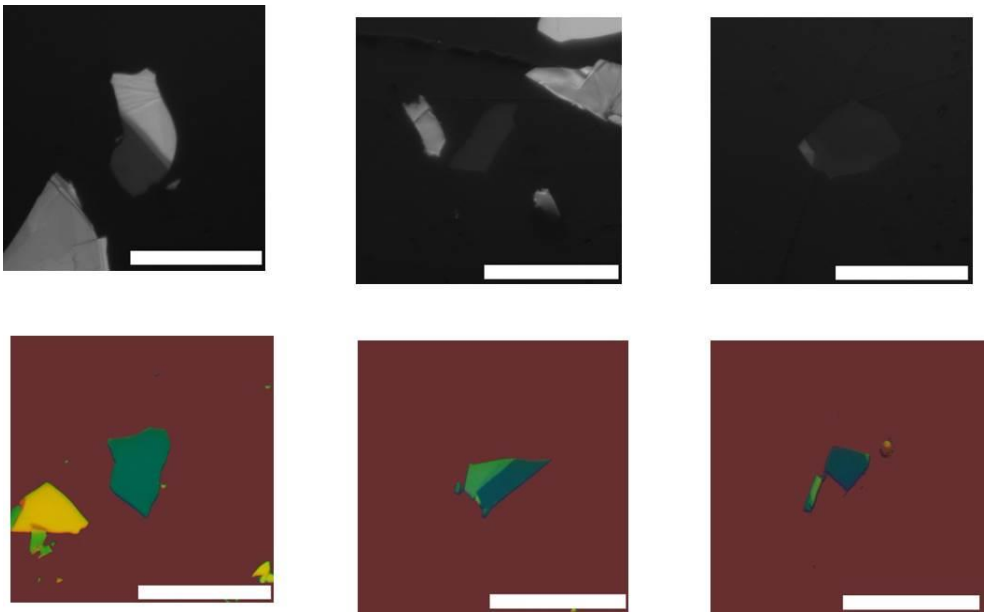

Figure 3.3. Bottom up transfer process. (a) BP and BN are exfoliated onto PDMS stamps. BN is exfoliated onto SiO_2. (b) The BP and BN are aligned and brought into contact, (c) the stamp is peeled away leaving the BP on the BN. (d) – (e) The process is repeated for the top BN until the completed hetero-structure is formed.

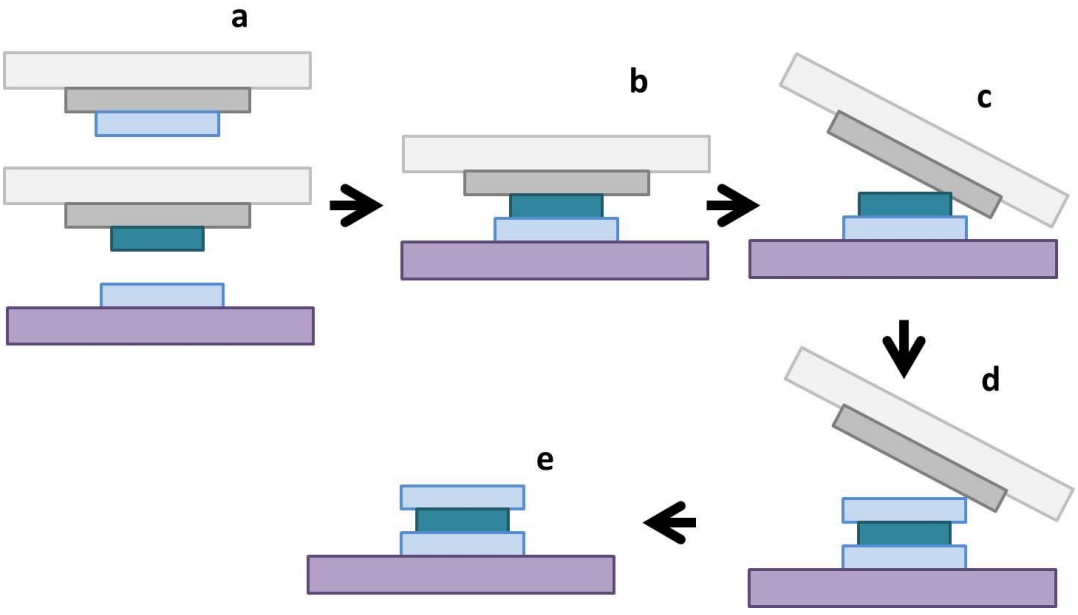

Figure 3.4. Top down transfer process. (a) BP and BN are exfoliated onto SiO_2. (b) A PDMS/PPC stamp is brought into contact then (c) the stamp is peeled quickly away lifting the BN from the SiO_2 substrate. (d) The process (b) – (c) is repeated for the BP. (e) In the last step, the BN-BP is aligned and brought into contact with the bottom BN. The stage is heated to 90 C and the stamp is removed leaving PPC and the hetero structure on the SiO_2 substrate. The PPC is removed in chloroform for 10 minutes.

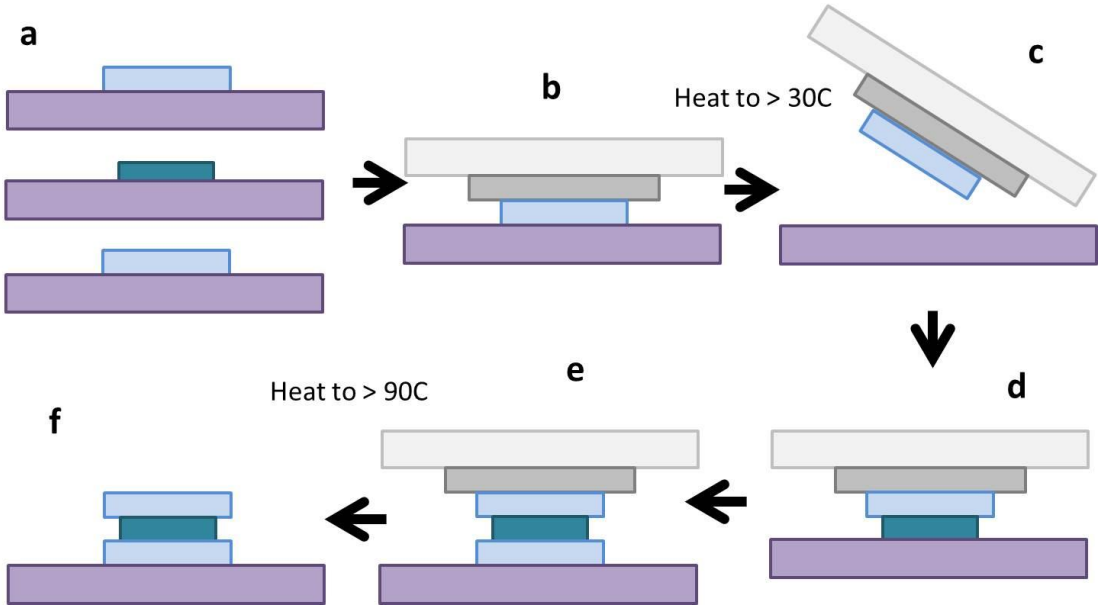

Figure 3.5. Schematics of edge profiles of (a) edge contact and (b) surface contact with partial surface etching.

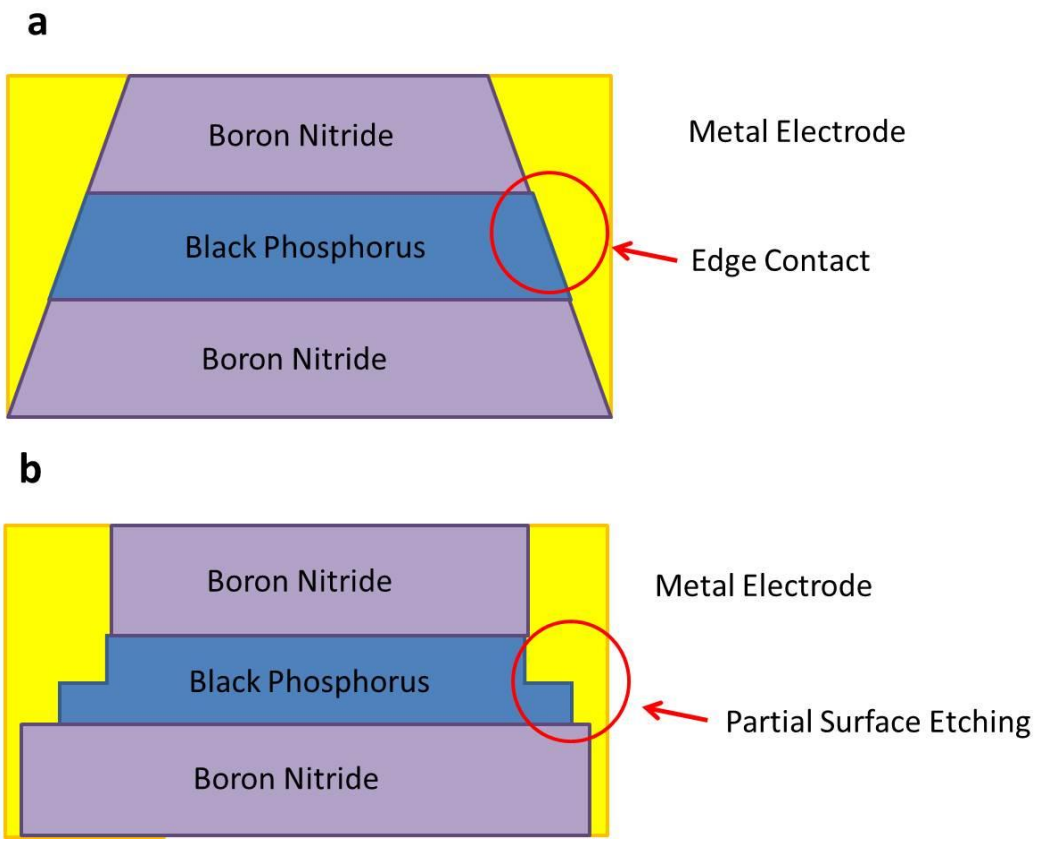

Figure 3.6. Typical Design pattern of BP device with 10 electrodes for gate and device contact. (a) Entire design showing bonding pads and alignment marks. (b) Close up view of electrode design showing various gates and etching patterns.

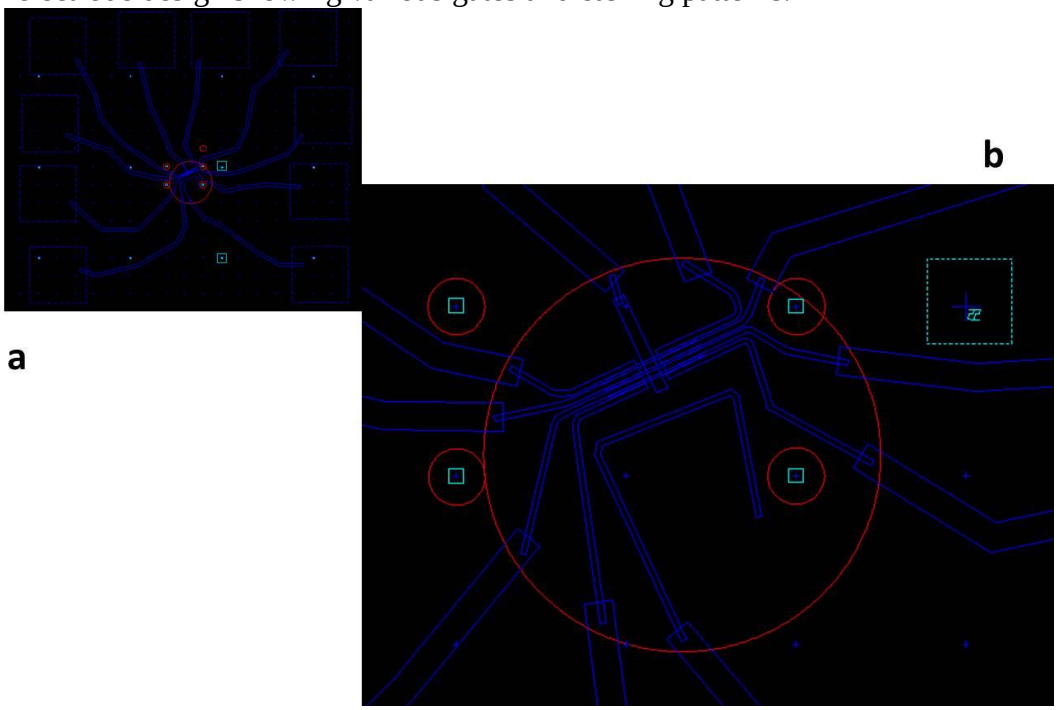

Chapter 4

Shubnikov de Haas Oscillations in 2D Black Phosphorus

4.1 Introduction and Overview

As discussed in chapter 1, the first generation of devices exhibited low mobilities relative to the bulk and were plagued with stability and mobility bottlenecks. Water assisted photo-oxidation degraded devices within hours and surfaces rapidly developed impurities. Both these impurities and substrate defects limited device mobilities to less than 1000 $cm^2V^{-1}s^{-1}$. Here, we address both challenges by utilizing the construction and fabrication techniques discussed in chapter 3. Such encapsulated devices are air-stable, exhibiting minimal degradation after more than 300 hours under ambient conditions. Electrical measurements on these BN/BP/BN heterostructures reveal ambipolar transport with on/off ratio exceeding 10^5 and mobility ~400 cm^2/Vs at room temperature. At low temperatures, device mobility increases to ~4000 cm^2/Vs. In magnetic field B>3.5T, gate-tunable SdH oscillations are observed, enabling the extraction of the cyclotron mass of few-layer phosphorene at different Fermi energies, ~0.25 to 0.31 m_e, where m_e is the rest mass of electrons. These values are in good agreement with those obtained from *ab initio* calculations. Finally, at B>8T, we observe a doubling of the SdH period, suggesting the emergence of Zeeman splitting and a g-factor of ~2. These results along with others demonstrated an order of magnitude improvement in device performance and paved the way for

the observation of the quantum hall effect in BP.

4.2 Stability of hBN-Encapsulated Devices

The devices consist of BN-BP-BN heterostructures that are fabricated using the techniques described in chapter 3 and are contact is made using partial etching method. To test the stability of hBN-encapsulated phosphorene devices, We monitor the two-terminal conductance *G vs.* back gate voltage V_{bg} for a device that is ~10 nm thick. A false-color optical image of the completed device is shown in figure 4.1(b) The red curve in Fig. 4.1c displays $G(V_g)$ measured immediately after fabrication; ambipolar transport is observed, with the charge neutrality point at V_g=-3V, and a field-effect mobility of ~ 30 cm^2/Vs. The device is kept in ambient conditions in a drawer and monitored after 24, 48, 72, 120, 192 and 312 hours. At the end of the period, the charge neutrality point shifts to 1V, suggesting a small increase in electron doping; the device conductance and mobility decreases only slightly. Such stability over nearly a fortnight constitutes enormous improvement over "bare" phosphorene samples, and is in fact better than most conventional graphene devices that are chemically stable and inert. Thus, with further optimization, phosphorene may be realistically employed for electronic and optoelectronic applications. Efforts by others also demonstrated improved stability using BN, aluminum oxide (AlO_x), and fluropolymers. Devices achieved electronic and physical stability from several weeks to several months.[1–3]

4.3 Transfer Characteristics and Mobility

Data from a ~10 nm-thick hBN-encapsulated phosphorene device in Fig. 4.2a-b presents the field-effect transistor behavior $G(V_g)$ at room temperature and low temperature, respectively. At temperature T=300K, the device exhibits ambipolar transport, an on/off ratio >10^5, sub-threshold swing of ~100 mV/decade in the hole regime, and hole mobility of ~ 400 cm^2/Vs (Fig. 4.2a). Unlike "bare" phosphorene devices[4], the $G(V_g)$ curves display minimal hysteresis, again underscoring device stability. At low temperature, the hole mobility increases to ~4000 cm^2/Vs at T=1.5K (Fig. 4.2b). Its current-voltage characteristics in the hole-doped regime remain linear at all temperatures (Fig. 4.2c), indicating ohmic contacts.

To further explore transport in the few-layer phosphorene device, We explore its conductance at different gate voltages as temperature varies. For highly hole-doped regime (V_g<-30V), the four-terminal longitudinal resistance R_{xx} decreases with decreasing temperature, indicating metallic behavior. However, as the Fermi level is tuned towards the band edge, *i.e.* for V_g>-25V, R_{xx} increases drastically as T is lowered, characteristic of an insulator (Fig. 4.2d). Fig. 4.2e plots $R_{xx}(T)$ for V_g=-70, -50, -30, -25, -20, -17 and -15V, respectively, where the clear dichotomy of gate-dependent metal-insulator transition is evident.

Further information on scattering mechanisms in the few-layer phosphorene device can be gleaned from the temperature dependence of mobility $\mu=\sigma/ne$. Here σ is the conductivity of the device, e the electron charge and n the

charge density. n can be extracted from geometrical considerations as well as magneto-transport data (see discussion below). Fig. 4.2f displays $\mu(T)$ for 3 different V_g values. When the Fermi level is deep in the valence band, μ increases with decreasing T for T>70K, but saturates at lower temperatures. The initial enhancement of μ is expected from phonon-limited scattering, where $\mu \sim T^{-\alpha}$. For atomically thin 2D materials, the exponent α is predicted to be ~1.69 for MoS_2[5], and between 1 to 6 for graphene[6–11]. For BP theoretical calculations predict α to be ~2 for phonon interactions[12] and ~0.3 for ionized impurity scattering[13]. The saturation of μ at lower temperatures suggests impurity-dominated scattering. When the Fermi level moves closer to the valence band edge (V_g>-25V), μ decreases with T; this behavior is discussed in chapter 6 where variable range hopping is identified as the dominant mechanism when the Fermi level is close to the band edge.

4.4 Quantum Oscillations

We now focus on transport behavior of the BP device in a perpendicular magnetic field. Fig. 4.3a plots ΔR_{xx}, in which a smooth background is subtracted from the longitudinal signal, as a function of V_g (vertical axis) and B (horizontal axis). Striking patterns of Shubnikov-de Haas (SdH) oscillations, appearing along straight lines that radiate from the charge neutrality point and B=0, are observable for B>3T. The charge neutrality point (or the center of the band gap) is extrapolated to be V_g^{CNP}~-28V. As discussed in chapter 2 these quantum oscillations arise from the Landau quantization of cyclotron motion of charge

carriers, and are often employed as a powerful tool to map Fermi surfaces of metals and semiconductors. The Lifshitz-Kosevich formula[14] discussed in chapter 2 describes these SdH oscillations.

$$\frac{\Delta R_{xx}}{R_{xx}} = \left(\frac{\hbar\omega_c}{2E_F}\right)^{1/2} \frac{\lambda}{sinh\lambda} e^{-\lambda_D} \cos\left(\frac{2\pi E_F}{\hbar\omega_c} + \frac{\pi}{4}\right) \qquad \square\square\square$$

In 2D systems with spin degeneracy, $\frac{2\pi E_F}{\hbar\omega_c} = 2\pi\frac{nh}{2Be}$, regardless of the details of the dispersion relation; thus the oscillations in resistance are periodic in *nh/2Be,* independent of m^*. The amplitudes of the oscillations scale with $n^{-1/2}$, and are also exponentially dependent on temperature and m^*. Fig. 4.3b displays line traces $\Delta R_{xx}(V_g)$ at constant B=2, 5, 8, 10 and 12T, where the oscillations are periodic in V_g. Fig. 4.3c plots ΔR_{xx} vs. B (left panel) and $1/B$ (right panel) at constant V_g=-30, -40 and -60V, respectively. As expected from Eq. (1), the oscillations grows in amplitude as the Fermi level moves towards the band edge, and the period is given by $1/B_F=2e/nh$. Using the oscillation data, We determine the back gate coupling efficiency to be ~ 8.0x10^{10} $cm^{-2}V^{-1}$, in reasonable agreement with that obtained from geometric considerations.

At large B>8T, we observe doubling of the oscillation frequency. This can be seen in the line traces in Fig. 4.3b-c, and in Fig. 4.3d that plots the high field portion of Fig. 4.3a, where the additional periods are indicated by arrows. Such doubling in frequency most likely arises from Zeeman splitting. At B=12T, its disappearance between 3K and 4.5K (see Fig. 4.4a) provides an upper bound for the Zeeman energy $g\mu_B B$, where g is the g-factor and μ_B Bohr magneton. Using

the simple estimate $g\mu_B B \sim k_B T$, We obtain g~1.8 to 2.7, which is reasonable.

We investigate the cyclotron mass of the charge carriers by measuring the temperature dependence of the oscillations. Fig. 4.4a presents $\Delta R_{xx}(V_g)$ at B=12T and different temperatures between 1.5K and 12K. The additional, Zeeman-induced oscillations disappear at T>~4K, and the main oscillations at T>15K. For a single period, the amplitude A of the main oscillation is measured by taking the average of the height between the peak and the two adjacent troughs. To extract m^*, we fit the T-dependence of the amplitudes to the temperature-dependent terms of the Lifshitz-Kosevich formula at constant E_F

$$\mathrm{A} = \frac{CT}{\sinh(bT)} \qquad (2)$$

where C and $b = \frac{2\pi^2 k_B m^*}{\hbar e}$ are fitting parameters (Fig. 4.4b). Reasonable agreement with data points are obtained, yielding m^* measured at different V_g values. As shown in Fig. 4.4c, $m^* \approx 0.31 m_e$ (m_e is the rest mass of electrons) at V_g=-30V or $n \approx -4.6\times10^{12}$ cm^{-2}. As V_g decreases to -64V ($n \approx -7.4\times10^{12}$ cm^{-2}), m^* becomes lighter ~$0.25 m_e$. This agrees with one's expectation that, as n increases and moves away from the band edge, the dispersion becomes flatter, thus resulting in smaller m^*.

Theoretically, as FLP are anisotropic, the effective masses along different principal axes are dramatically different. The cyclotron mass extracted from SdH oscillations is the geometric mean of those along different axes in the x-y plane, $m^* = \sqrt{m_x^* m_y^*}$. In Gillgren et al.[15] they use density functional theory (DFT)

implemented in the Vienna Ab-initio Simulation Package (VASP) to calculate the valence band effective masses along the k_x and k_y direction for the experimentally explored range of density for FLP with different thicknesses. As n decreases and E_F moves towards the band edge, m_x^* remain fairly constant, 0.11-0.12m_e for all thickness; in contrast, m_y^* exhibits strong dependence on number of layers and on E_F. For instance, at n=-4.8x10^{12} cm^{-2}, m_y^*/m_e=6.2 for monolayer phosphorene, and 2 for 25 layers; this value decreases to 4.4 and 1.2, respectively, at n=-8x10^{12} cm^{-2}. Fig. 4.4d plots the theoretically calculated cyclotron mass $\sqrt{m_x^* m_y^*}$ as a function of V_g. All FLP of different thicknesses exhibit the general trend of increasing m^* towards the band edge, as observed experimentally. The theoretically calculated m^* agrees with the experimentally measured values within 50%, which is reasonable.

4.5 Conclusion

These results demonstrate the efficacy of BN/BP/BN heterostructures in improving BP device stability and performance. We observe a record mobility of 4000 cm^2/Vs and a gate-tunable metal-insulator transition. At low temperatures SdH osillations enable the measurement of the effective mass with carrier density and Zeeman-split landau levels reveal a g-factor of ~2.

Apart from our work, several parallel studies created passivation techniques to stabilize BP devices. Wood *et al* deposited aluminum oxide (AlO_x) onto bare BP devices on silicon substrates, which preserved device performance for over 2 weeks under ambient conditions.[1] AlO_x and hydrophobic

fluoropolymer were successfully implemented by Kim et al in creating air-stable devices for over 100 days.[2] Avsar *et al* used BN to stabilize BP devices contacted by graphene.[3] These studies highlight the diverse techniques that created air-stable BP devices. Our own devices were stable for 2 weeks and showed limited device degradation which is similar to the studies above. However, while AlO_x and fluoropolymers solved stability problems they do not improve device mobility.

Several other studies also reported SdHO.[16–19] With the exception of Tayari et al, these studies employed BN as a high quality substrate to improve device mobility. Cao *et al* and Chen *et al* encapsulated their devices with BN, while Tayari *et al* employed a polymer encapsulation technique and Li *et al* did not utilize any encapsulation technique. Apart from our devices that allowed the observation of SdHO at as low as 3T, the lowest observed onset of SDHO amongst these studies was at 6T, with the rest observing at above 8T. Li *et al* reported effective mass for both electron and holes with values of 0.48 m_e and 0.35m_e respectively. Cao *et al* reported hole effective mass of 0.24 m_e. Li *et al* determine that the *g*-factor ranges between 2.13 – 2.94 and Cao *et al* measured g to be 2.3. These results agree reasonably well with our studies presented in this chapter, they highlight the explosive interest into BP research, and they paved the way for the observation of the quantum Hall effect.

The quantum Hall effect in BP was first reported by Li *et al* in May 2015 by employing a graphene gate which screened the impurity potential in the BP

2DEG.[20] Under tilted magnetic fields, they explored the spin-split landau levels so that spin-split Landau levels cross in a tilted magnetic field, revealing that the Zeeman energy is a significant fraction of the cyclotron energy. Long *et al* later improved device quality even further by fabricating devices in vacuum and achieving a field-effect mobility of 45,000 $cm^2V^{-1}s^{-1}$, though the quantum mobility is much lower and estimated to be ~ 4,000 $cm^2V^{-1}s^{-1}$.[21] They observed the quantum hall effect with filling factors down to $\nu = 2$, effective mass of 0.26 m_e, and a *g*-factor of 2.47. Members from our own group also observed the quantum hall effect in a double quantum well structure.[22] We observed fully spin-polarized quantum hall states and an enhanced *g*-factor that is attributed to exchange interactions. These results highlight the exciting new possibilities in BP research with devices achieving record mobility that allow for the exploration of new and exciting physics.

References

1. Wood, J. D. *et al.* Effective Passivation of Exfoliated Black Phosphorus Transistors against Ambient Degradation. *Nano Lett.* **14,** 6964–6970 (2014).

2. Kim, J.-S. *et al.* Toward air-stable multilayer phosphorene thin-films and transistors. *Sci. Rep.* **5,** 8989 (2015).

3. Avsar, A. *et al.* Air-Stable Transport in Graphene-Contacted, Fully Encapsulated Ultrathin Black Phosphorus-Based Field-Effect Transistors. *ACS Nano* **9,** 4138–4145 (2015).

4. Koenig, S. P., Doganov, R. A., Schmidt, H., Castro Neto, A. H. & Özyilmaz, B. Electric field effect in ultrathin black phosphorus. *Appl. Phys. Lett.* **104,** 103106 (2014).

5. Kaasbjerg, K., Thygesen, K. S. & Jacobsen, K. W. Phonon-limited mobility in n-type single-layer MoS${}_{2}$ from first principles. *Phys. Rev. B* **85,** 115317 (2012).

6. Hwang, E. H. & Das Sarma, S. Acoustic phonon scattering limited carrier mobility in two-dimensional extrinsic graphene. *Phys. Rev. B* **77,** 115449 (2008).

7. Mariani, E. & von Oppen, F. Temperature-dependent resistivity of suspended graphene. *Phys. Rev. B* **82,** 195403 (2010).

8. Mariani, E., Pearce, A. J. & von Oppen, F. Fictitious gauge fields in bilayer graphene. *Phys. Rev. B* **86,** 165448 (2012).

9. Ochoa, H., Castro, E. V., Katsnelson, M. I. & Guinea, F. Temperature-dependent resistivity in bilayer graphene due to flexural phonons. *Phys. Rev. B* **83,** 235416 (2011).

10. Min, H., Hwang, E. H. & Das Sarma, S. Chirality-dependent phonon-limited resistivity in multiple layers of graphene. *Phys. Rev. B* **83,** 161404 (2011).

11. Castro, E. V. *et al.* Limits on Charge Carrier Mobility in Suspended Graphene due to Flexural Phonons. *Phys. Rev. Lett.* **105,** 266601 (2010).

12. Trushkov, Y. & Perebeinos, V. Phonon-limited carrier mobility in monolayer black phosphorus. *Phys. Rev. B* **95,** 75436 (2017).

13. Liu, Y. & Ruden, P. P. Temperature-dependent anisotropic charge-carrier

mobility limited by ionized impurity scattering in thin-layer black phosphorus. *Phys. Rev. B* **95,** 165446 (2017).

14. Ando, T., Fowler, A. B. & Stern, F. Electronic properties of two-dimensional systems. *Rev. Mod. Phys.* **54,** 437–672 (1982).

15. Gillgren, N. *et al.* Gate tunable quantum oscillations in air-stable and high mobility few-layer phosphorene heterostructures. *2D Mater.* **2,** 11001 (2014).

16. Li, L. *et al.* Quantum oscillations in a two-dimensional electron gas in black phosphorus thin films. *Nat. Nanotechnol.* **10,** 608–13 (2015).

17. Tayari, V. *et al.* Two-dimensional magnetotransport in a black phosphorus naked quantum well. *Nat. Commun.* **6,** 7702 (2015).

18. Chen, X. *et al.* High-quality sandwiched black phosphorus heterostructure and its quantum oscillations. *Nat. Commun.* **6,** 7315 (2015).

19. Cao, Y. *et al.* Quality Heterostructures from Two-Dimensional Crystals Unstable in Air by Their Assembly in Inert Atmosphere. *Nano Lett.* **15,** 4914–4921 (2015).

20. Li, L. *et al.* Quantum Hall Effect in Black Phosphorus Two-dimensional Electron Gas. (2015). at <http://arxiv.org/abs/1504.07155>

21. Long, G. *et al.* Achieving Ultrahigh Carrier Mobility in Two-Dimensional Hole Gas of Black Phosphorus. *Nano Lett.* **16,** 7768–7773 (2016).

22. Tran, S. *et al.* Surface Transport and Quantum Hall Effect in Ambipolar Black Phosphorus Double Quantum Wells. (2017). at <http://arxiv.org/abs/1703.04911>

Fig. 4.1. (a). Atomic configuration of monolayer phosphorene. (b). False-color optical microscope image of a completed device. Inset: schematic of the device's side view. (d). Two-terminal conductance G of a hBN/FLP/hBN heterostructure *vs.* gate voltage V_g. The different traces correspond to data taken successively after different hours of exposure to ambient conditions.

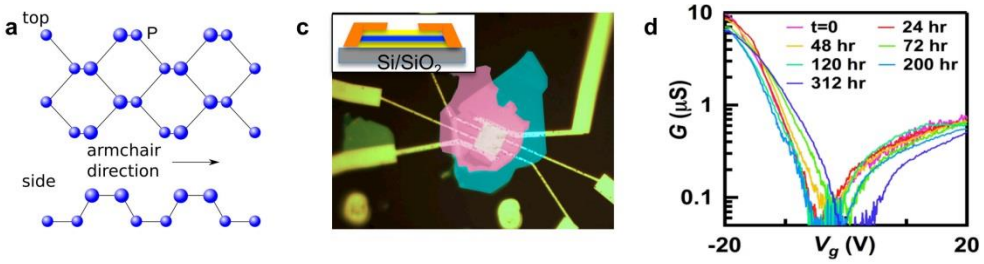

Fig. 4.2. Transport data at B=0. (a-b). $G(V_g)$ of a 10-nm-thick hBN/FLP/hBN heterostructure at T=300K and 1.5K, respectively. The two curves in (a) correspond to different sweeping direction. (c). Current-voltage characteristics at T=1.6K and different gate voltages. (d). Four-terminal resistance R_{xx} vs. V_g at different temperatures. (e). $R(T)$ at V_g= 70, -50,-30, -25, -20, -17 and -15V, respectively (bottom to top). (f). Mobility $\mu(T)$ for V_g=-70, -25 and -15V.

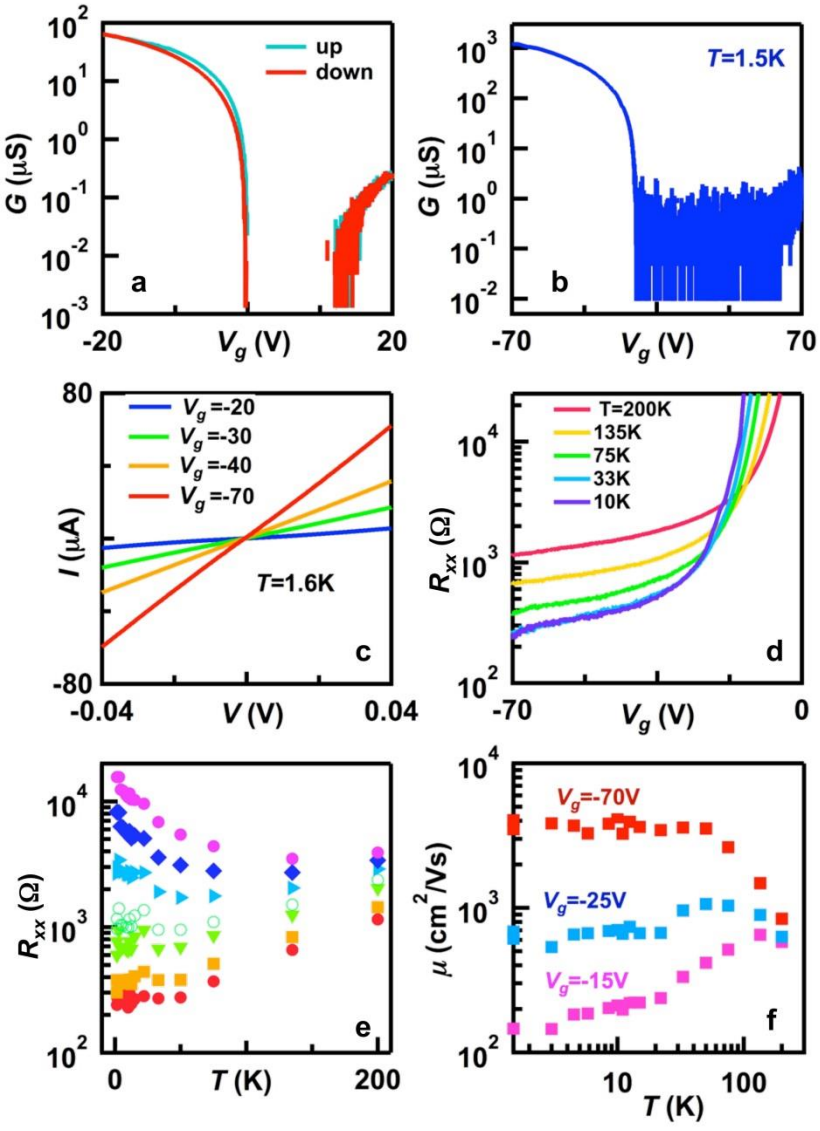

Fig. 4.3. (a). Oscillations ΔR_{xx} (color) vs. V_g and B. A smooth background is subtracted from the resistance data. (b). $\Delta R_{xx}(V_g)$ at different magnetic fields. The traces are offset for clarity. (c). ΔR_{xx} vs. B (left) and $1/B$ (right) at different V_g. The traces are offset for clarity. (d). A zoom-in plot of the oscillations $\Delta R_{xx}(V_g, B)$ in high fields. The arrows indicate the appearance of the second period induced by Zeeman splitting.

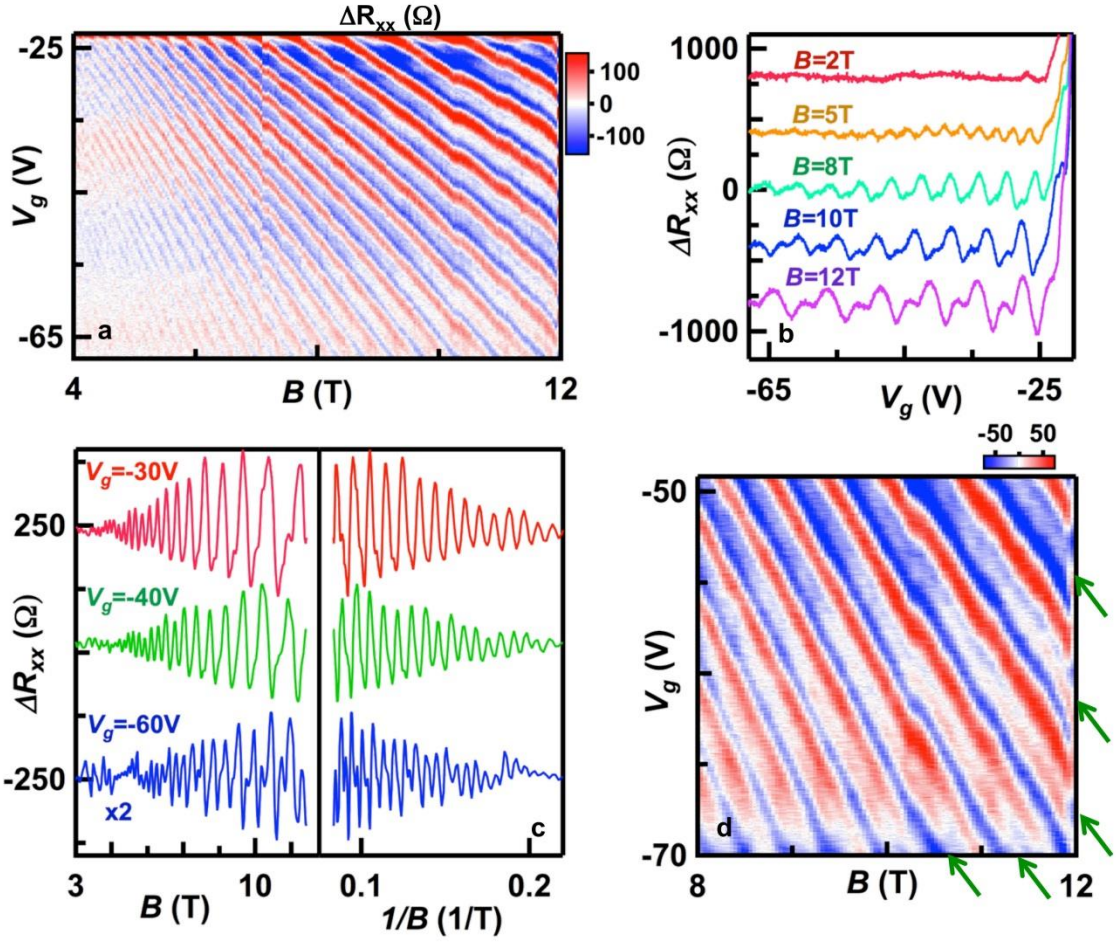

Fig. 4.4. (a). $\Delta R_{xx}(V_g)$ taken at B=12T and T=1.5, 3, 4.5, 5.8, 7, 8.5, 10, 11, 12.5 and 15K, respectively (bottom to top). (b). Data points are measured oscillation amplitude vs. T for the peaks at V_g= -30, -36, -43, -50,-57, -64V, respectively (bottom to top). The lines are fits to Eq. (2). The traces in (a) and (b) are offset for clarity. (c). Extracted cyclotron mass from SdH oscillations as a function of V_g. (d). Cyclotron masse $\sqrt{m_x^* m_y^*}$ from DFT calculations for FLP with different number of layers.

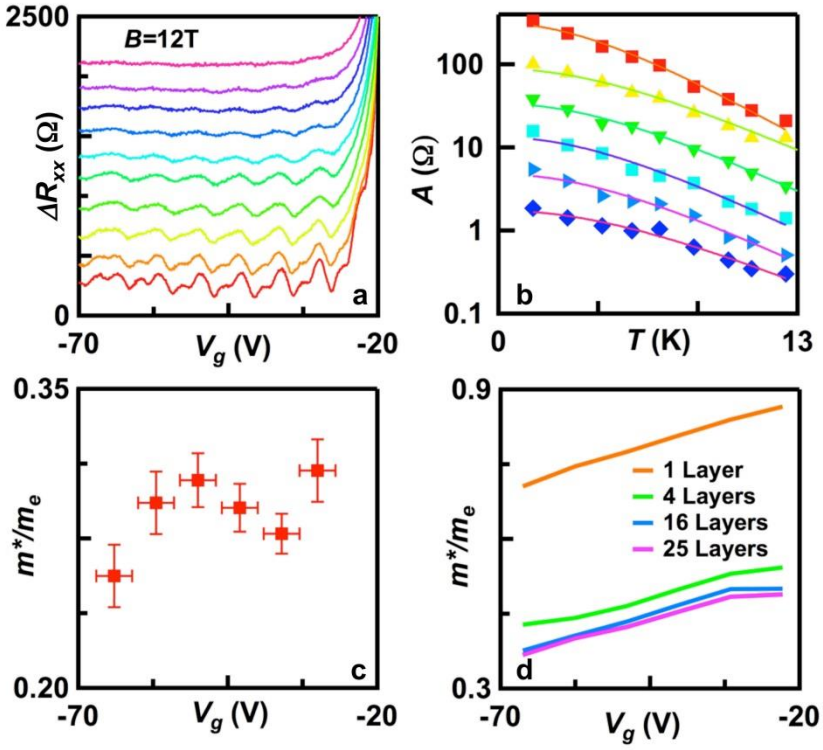

Chapter 5

Weak Localization and Electron-electron Interactions in Few Layer Black Phosphorus Devices

5.1 Introduction and Overview

Scattering mechanisms in layered BP were not fully explored in the first generation of devices. In this chapter, we present magneto-transport studies at low temperatures. From weak localization measurements, we estimate the electron dephasing length to be 30 to 100 nm, which exhibits a strong dependence on carrier density n and a power-law dependence on temperature ($\sim T^{-0.4}$). These results establish that the dominant scattering mechanism in FLP is electron-electron interactions.

5.2 Transfer characteristics and mobility

Here we present transport data from two different devices that are ~ 20 nm thick, with mobility up to 1700 cm^2/Vs. An optical image of a typical device is shown in figure 5.1(a). Devices were fabricated as described in chapter 3 with both devices encapsulated in BN. Device 1 was contacted with edge contacts and device 2 was contacted with partial etching. BP has a thickness-dependent band gap[1]. For BP that are more than 5 layers, the gap is similar to that of bulk, ~ 0.3 eV[1]. Fig. 5.1b displays the two-terminal conductivity σ of device A as a function of applied gate voltage (V_g) at T=300mK, and Fig. 5.1c displays the four-terminal conductivity of device B at T=1.5K. σ~0 for both devices, when the Fermi level is within the band gap. For V_g<-15V, σ increases linearly (device A) or superlinearly (device B) with V_g, indicating hole mobility of ~ 500 cm^2/Vs

and 1700 cm^2/Vs, respectively. We note that the apparent doping of the device, *i.e.* the offset of the charge neutrality points from zero gate voltage, may result from the charge transfer from PDMS during the fabrication process, or presence of small amount of impurities on the hBN sheets. In both devices, conductivity of electron-doped regime is significantly lower, which is likely due to the formation of Schottky barriers at electrode-BP interfaces. Hence we focus on transport properties in the *p*-doped regime.

In the highly *p*-doped regime, device conductivity significantly exceeds σ_q, where $\sigma_q=e^2/h\sim39\ \mu$S is the conductance quantum, thus the device is in the metallic regime (here h is Planck's constant, e the electron charge). However, σ decreases slightly with T. As discussed in chapter 2 this is a signature of electron interactions in disordered 2D thin films. In fact, σ is expected to exhibit a logarithmic dependence on T,

$$\sigma = \sigma_0 + C\frac{2e^2}{\pi h}\ln(\frac{T}{T_0}) \qquad (1)$$

where σ_0 is the "intrinsic" metallic conductivity, T_0 is a characteristic temperature estimated to be $\hbar/k_B\tau_0$, k_B the Boltzmann's constant, τ_0 the electron scattering time, and C a dimensionless constant that is of order unity depending on the scattering mechanism[2]. This logarithmic dependence is borne out by experimental data from device B, shown as circles in Fig. 5.1d. At charge density $n\sim -1.75\text{x}10^{16}\ m^{-2}$, $\sigma_0\sim0.4$ mS, and using effective mass $m^*\sim0.26\ m_e$[3], τ_0 is estimated from Drude model to be ~0.21 ps, yielding $T_0 \sim 36$ K. The dashed line is a fit to Eq. (1) with $C\sim1.6$ as the fitting parameter, in agreement with theory. (Device A was only measured at T=0.3K and 1.5K, where conductivity remains intrinsic and constant).

5.3 Weak Localization

To further explore the inelastic scattering mechanism, we employ weak localization measurements by applying a perpendicular magnetic field B. As discussed in chapter 2 weak localization (WL) is the quantum correction to the classical conductivity of a diffusive system[4,5]. In a 2D system, due to multiple inelastic scatterings, electrons in a closed trajectory interfere constructively with the time-reversed path, resulting in enhanced backscattering and hence lower conductivity. Application of a small B destroys the interference, thus conductivity increases. WL has been widely applied to 2D systems for measuring the inelastic scattering time, characterized by the dephasing time τ_φ. When the elastic scattering time is much shorter than the inelastic scattering time, the change in magnetoconductance induced by B is given by[5,6]

$$\Delta\sigma = \sigma(B) - \sigma(B=0) = -\frac{e^2}{\pi h}\left[ln\left(\frac{B_\varphi}{B}\right) - \Psi\left(\frac{1}{2}+\frac{B_\varphi}{B}\right)\right] \qquad (2)$$

where σ is the device conductivity, h is Planck's constant, e is the electron charge, Ψ is the digamma function, $B_\varphi = \frac{\hbar}{4eL_\varphi^2}$ is the magnetic field required to destroy phase coherence, $L_\varphi=\sqrt{D\tau_\varphi}$, and D is the diffusion coefficient.

Figure 5.2a displays the normalized conductivity $\Delta\sigma$ in units of $\frac{e^2}{\pi h}$ (color) as a function of n (vertical axis) and B (horizontal axis). As B is swept from -0.8T to +0.8T, $\Delta\sigma$ displays positive magnetoconductivity with a minimum at B=0T, consistent with the time reversal symmetry breaking of phase coherent back scattering. The magnitude of $\Delta\sigma$ is relatively large (>1) when the device is highly doped, and small (<0.1) when the Fermi level is close to the band edge. Representative line traces $\Delta\sigma$ (n) are shown as solid lines

in Fig. 5.2b, and the dashed lines are fits using Eq. (2). Satisfactory agreement between the data and Eq. (2) are obtained. From the fitting parameter B_φ, we obtain $L_\varphi \sim 75$ nm at n=-1.8 x 10^{12} cm^{-2}. Using $D=\frac{\hbar}{4m^*}\frac{\sigma}{\sigma_q} \sim 4.3\text{x}10^{-4}$ m^2/s, the inelastic scattering time is estimated to be $\tau_\varphi \sim$13 ps, which is two orders of magnitude longer than the elastic scattering time τ_0. This is consistent with the applicability condition of Eq. (2), and establishes that charge transport in these FLP devices is diffusive but phase coherent over tens of nanometers. Similar calculations yield that, at n=-1.0 and -0.7x10^{12}cm^{-2}, $L_\varphi \sim 60$ nm and 40 nm and $\tau_\varphi \sim$ 8.4ps and 3.7ps, respectively.

To explore the scattering mechanism, we examine the temperature dependence of L_φ in device B. In general, the dephasing time $\tau_\varphi \sim T^{-\alpha}$, where the exponent α depends on the scattering mechanisms. In particular,α~2 for electron-phonon scattering. On the other hand, if electron-electron interaction is the dominant mechanism, two separate processes may occur depending on the impurity density of the system[5,7] -- the first involves direct scattering between electrons and large momentum transfer, with a rate that scales with $(k_BT)^2$, so α=2; the second process involves small momentum transfer, and considers not individual collision events but instead the interaction of an electron with the fluctuating electromagnetic environment produced by the movement of other electrons. The latter process is similar to that in the Nyquist noise, with a rate that scales linearly with k_BT in 2D, hence α=1[5]..

Figure 5.3 displays $L_\varphi(T)$ at four different hole densities. As expected, L_φ increases as T decreases from 15K to 2K, then saturates for T<2K. We fit the data points above 2K to a power law dependence $L_\varphi \sim T^{-\beta}$. The measured values of $\beta = \alpha/2$ are found

to be ~ 0.4 ± 0.02 for all densities, which is close to the value of β=0.5 or α=1 expected from the theory of electronic interactions with small momentum transfer. Quantitatively, the Altshuler-Aronov-Khmelnitsky theory predicts $\frac{\hbar}{\tau_\varphi} = \frac{k_B T}{\sigma/\sigma_q} ln(\sigma/\sigma_q)$ [5]. Combined with the expression for D, the dephasing length is given by

$$L_\varphi = \frac{\hbar\sigma}{\sigma_q}\left[ln(\sigma/\sigma_q)4m^* k_B T\right]^{-1/2} \qquad (3)$$

From Eq. (1), σ exhibits a weak logarithmic dependence on T, thus L_φ should scale with $T^{-1/2}\ln(T)$, and the ln(T) term accounts for the observed deviation of β from the expected value of 0.5. Thus the $L_\varphi(T)$ data establish that the main dephasing mechanism at low temperatures arise from electron-electron interactions with small momentum transfer, though the saturation of L_φ at T<2K may suggest a different mechanism at ultra-low temperatures.

Lastly, we explore the dependence of L_φ on charge density. Fig. 5.4a plots $L_\varphi(n)$ for device A at T=0.3K, and that for device B at T=1.5K and 4K. Clearly, L_φ is strongly dependent on carrier density, varying by almost 1 order of magnitude from 30 nm to 110 nm when n increases from 0.5 to 2x10^{12} cm^{-2}. In fact, L_φ appears to have power-law dependence on n, $L_\varphi \sim n^p$, where p appears to be less than 1 for device A at T=300 mK, and ~1.5 and 2 for device B at T=1.5K and 4K, respectively.

Such $L_\varphi(n)$ dependence can be readily understood from Eq. (3), which shows that L_φ should be slightly superlinear in σ, and the latter is in turn linear or superlinear in n. This is explicitly verified by plotting L_φ/σ for device A at T=0.3 K and device B at T=1.5K and 4K, respectively (Fig. 5.4b). All 3 curves are relatively independent of n at

relatively high hole density. The slight rises in the curves at lower carrier density is attributed to the larger Schottky barriers and increasing contact resistance towards the band edge. This deviation is largest in the two-terminal data of Device A, and much smaller but still present in the *invasive* four-terminal data of Device B. Taken together, these results again confirm that inelastic scattering processes at low temperature in FLP are dominated by electron-electron interactions.

5.4 Conclusion

In short, we have observed the weak localization in hBN-encapsulated FLP devices. The dephasing length is measured to be ~30 to 100 nm, and exhibits power-law dependences on temperature and charge density. Our results demonstrate that the main dephasing mechanism in these few layer BP devices is electron-electron interactions with small momentum transfer.

Weak localization in layered BP with thickness 5 – 10 nm was first reported by Du *et al* on silicon substrate with no encapsulation.[8] They measured gate tunable phase relaxation lengths between 30 nm – 110 nm and a temperature dependence which scaled as $T^{-0.5}$. Hemsworth *et al* observed phase relaxation lengths from 20 – 70 nm SiO_2 substrates with polymer encapsulation, but measured a temperature dependence which scaled as $T^{-1/3}$.[9] This was compared with quasi-one dimensional weak localization which has a de-phasing time constant tau which scales as $T^{-2/3}$ and found that the de-phasing times in their samples followed a similar trend. While still unclear they attributed this quasi-one dimensional transport to the puckered crystal structure of BP layers. Phase relaxation lengths between 20 – 200 nm were reported by Long et al on BN encapsulated

devices with a temperature dependence which scaled as $T^{-0.48}$.[10] Our own results here demonstrate rather good agreement with both Du et al and Long et al, measuring similar phase relaxation lengths and temperature dependences. These results across both different substrates and encapsulations would indicate these results are intrinsic to layered BP. Considering Hemsworth's results, it should be noted that they were the only group to encapsulate their devices with a polymer, which could affect their observed temperature dependence by adding a source of disorder.

References

1. Warschauer, D. Electrical and Optical Properties of Crystalline Black Phosphorus. *J. Appl. Phys.* **34,** 1853 (1963).

2. Ando, T., Fowler, A. B. & Stern, F. Electronic properties of two-dimensional systems. *Rev. Mod. Phys.* **54,** 437–672 (1982).

3. Gillgren, N. *et al.* Gate tunable quantum oscillations in air-stable and high mobility few-layer phosphorene heterostructures. *2D Mater.* **2,** 11001 (2014).

4. Hikami, S., Larkin, A. I. & Nagaoka, Y. Spin-Orbit Interaction and Magnetoresistance in the Two Dimensional Random System. *Prog. Theor. Phys.* **63,** 707–710 (1980).

5. Altshuler, B. L., Aronov, a G. & Khmelnitsky, D. E. Effects of electron-electron collisions with small energy transfers on quantum localisation. *J. Phys. C Solid State Phys.* **15,** 7367–7386 (2000).

6. Bergmann, G. Weak Localization in Thin Films. *Phys. Scr.* **T14,** 99–99 (2007).

7. Fukuyama, H. & Abrahams, E. Inelastic scattering time in two-dimensional disordered metals. *Phys. Rev. B* **27,** 5976–5980 (1983).

8. Du, Y., Neal, A. T., Zhou, H. & Ye, P. D. Weak Localization in Few-Layer Black Phosphorus. (2016). at <http://arxiv.org/abs/1602.03608>

9. Hemsworth, N. *et al.* Dephasing in strongly anisotropic black phosphorus. *Phys. Rev. B* **94,** 245404 (2016).

10. Long, G. *et al.* Gate-tunable strong-weak localization transition in few-layer black phosphorus. (2017). at <http://arxiv.org/abs/1702.04093>

FIG. 5.1 (a) An optical image of a typical hBN-encapsulated FLG device with hall bar geometry and a top gate. Scale bar: 10 μm. (b) Two-terminal conductivity as a function of back gate voltage of device A at T = 0.3K. (c) Four-terminal conductivity as function of back gate voltage of device B at T = 1.5K. (d) The conductivity of device B as function of temperature taken at V_{bg} = -35V. The dashed line is a fit to Eq.(1).

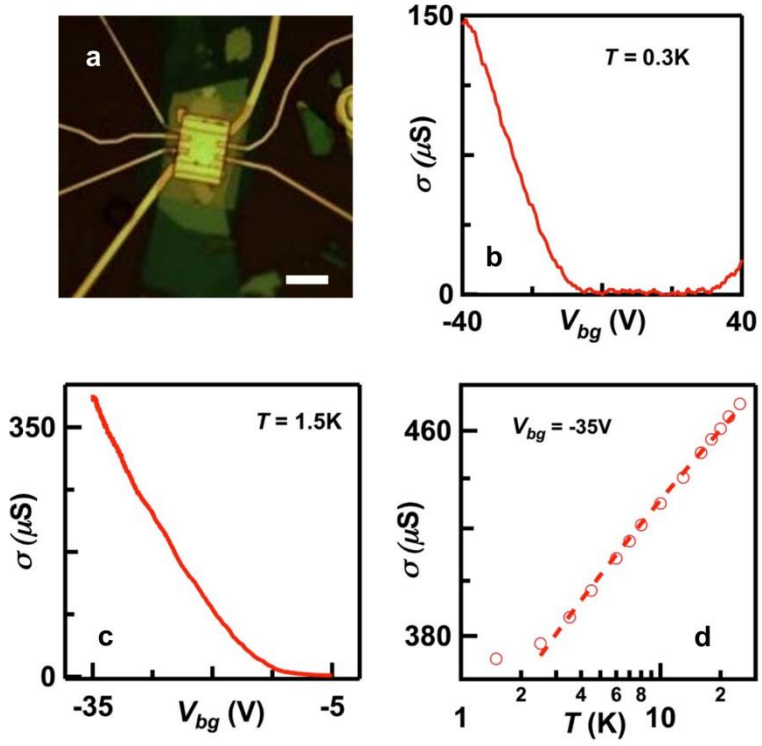

FIG. 5.2 Weak localization data from device A. (a). Normalized conductivity $\Delta\sigma$ in units of $e^2/\pi h$ vs. carrier density and magnetic field. Note that below $-0.38\text{x}10^{-12}$ cm^{-2} the device no longer displays the suppression of weak localization. This is attributed to the device entering the insulating state. (b) Solid lines: line traces $\Delta\sigma(B)$ at -1.8, -1, and -0.7 $\text{x}0^{-12}\text{cm}^{-2}$, respectively (top to bottom). Dotted lines: fits to the data using Eq.(2).

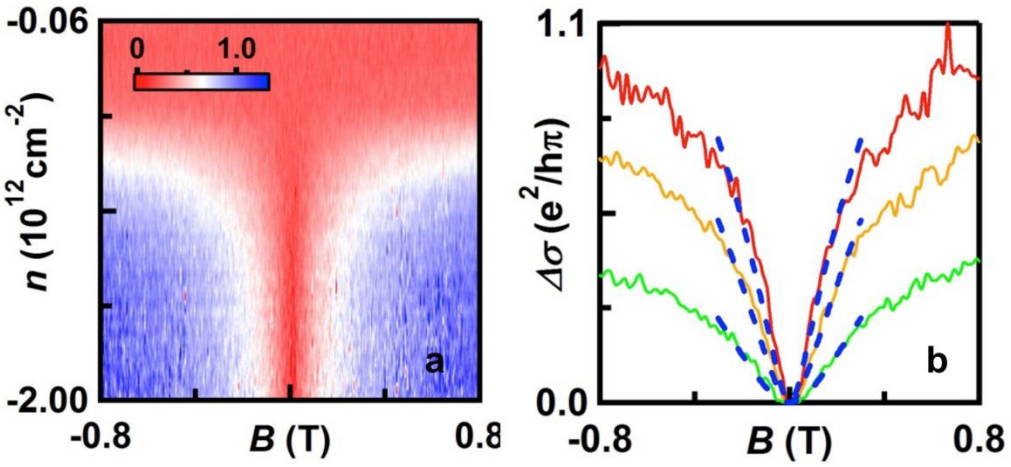

FIG. 5.3 Temperature dependence of dephasing length of device B at different hole densities. Dashed lines are fits to power-law dependence $T^{-0.4}$

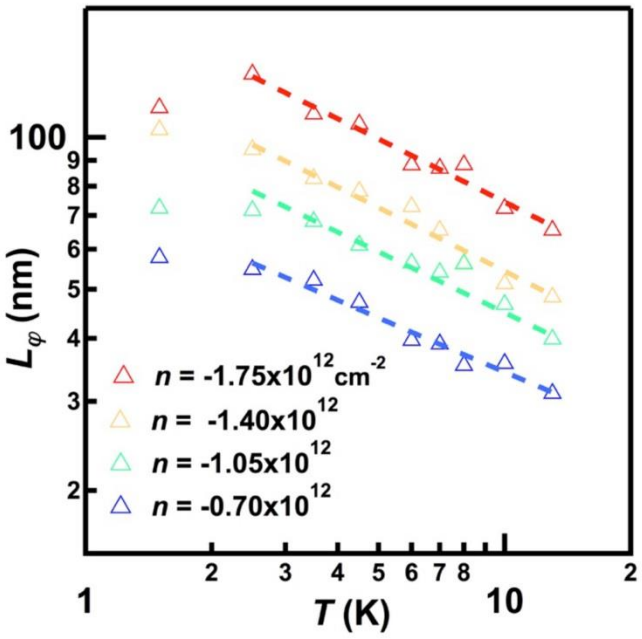

FIG. 5.4 (a) The dependence of dephasing length L_φ on carrier density from Device A at 0.3K(blue), and Device B at 1.5K (red) and 4K (green) respectively. (b) $L_\varphi/\sigma\ (n)$ for the devices, where σ is taken from B=0 measurements.

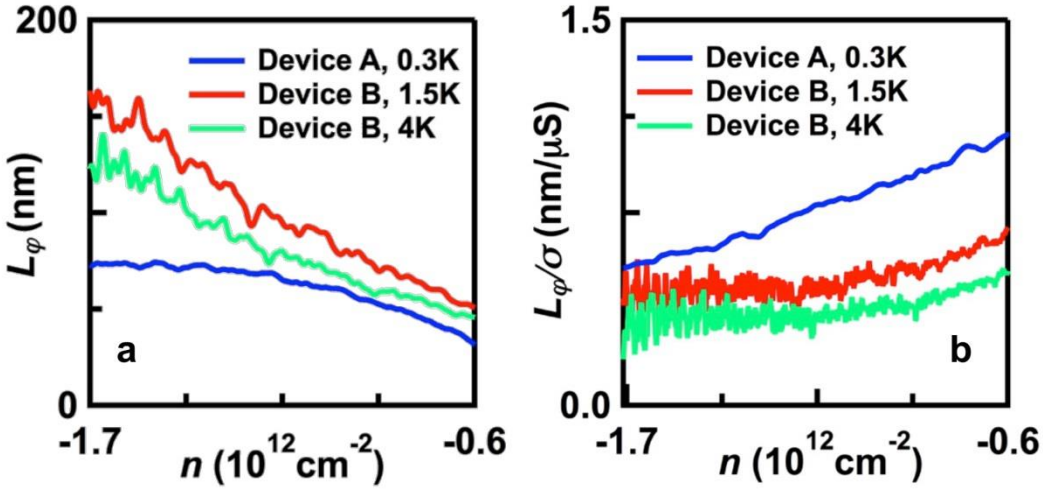

Chapter 6

Mobility and Transport Mechanism

in Black phosphorus – Boron Nitride Heterostructures

6.1 Introduction and overview

In the previous chapters, we explored the low temperature magnetic field transport properties in BP-BN heterostructure devices in the metallic regime, and observed quantum oscillations, improved mobility, and density dependent phase relaxation lengths. This chapter explores transport in BP-BN devices in the semiconducting regime at temperatures up to 300K. We demonstrate orders of magnitude control over the transfer curve properties, including a factor of 10^3 increase in on/off ratios and 10^2 in modulation of conductance. In gate configurations where the device displays metal-like temperature transport, we identify ionic conduction as the limiting scattering mechanism. Variable temperature measurements in the semiconducting regime demonstrate transport variable range hopping, with estimated localization lengths ~ 3-30 nm.

6.2 Device Fabrication and Geometry

We fabricated our devices using techniques described in chapter 3. A micrograph of the devices used in this study is shown in figure 6.1a. A schematic of the ideal device architecture is provided in figure 6.1c. Charge density of the center region of the BP sheet is controlled by a local graphite gate; since it screens the electric field from the silicon back gate, the latter only modulates the charge densities of the two outer regions. Thus

the density and polarity of charge carriers in the central and outer region can be adjusted independently. All measurements were acquired in a Janis Liquid He cryostat with variable range temperature controls using standard lock-in amplifier techniques

Figure 6.1b shows a typical device transfer curve of the conductance G as a function of inner gate V_{inner} at a fixed outer gate V_{outer} = -50V taken at 0V bias with lock-in amplifier and T = 1.5k. When both gates are negative (positive), the device becomes a p-p'-p (n-n'-n) junction. Since three regions have the same charge polarity, the device is relatively conductive. When the two gate voltages have different polarities, the device becomes a p-n-p or n-p-n junction, and is insulating. The data clearly demonstrates high conductance modulation, high mobility of ~500 $cm^2V^{-1}s^{-1}$, and a large on-off ratio of > 10^5 that is limited by the -noise floor of the amplifier in our measurements.

Since the device displays higher conductance when hole-doped, we will focus on the p-p'-p regime. Figure 6.2b-c displays $G(V_{inner})$ at constant V_{outer} ranging from -9V to +9V, and figure 6.2d displays $G(V_{outer})$ at constant V_{inner}. Here the device can be simply approximated as three resistors in series $G = (2/G_{outer} + 1/G_{inner})^{-1}$, where G_{inner} and G_{outer} are the conductance of the inner and outer regions, respectively. As expected, G increases with either increasing G_{inner} or G_{outer}, which is reflected in the above curves.

6.3 Mobility

We now explore the disorder and transport mechanisms in the p-p'-p regime. To this end, we measure current as both voltage bias and temperature are varied, while keeping V_{inner} and V_{outer} at constant voltages (V_{inner}, V_{outer}) – (-8, -40) V, (-7, -30) V, (-6, -20) V, (-5, -12) V, (-4, -4) V, as marked on figure 6.3a. For the first 2 gate configurations,

the device is metallic, i.e. its conductance increases as temperature decreases. Generally, in the metallic regime, device mobility (and hence conductance) is expected to follow $\mu \sim T^{\alpha}$, where the exponent α depends on the dominant scattering mechanism. In figure 6.3b we show the log-log plot of G as a function of temperature T at gate configurations (-7,-30) and (-8,-40), where α is measured to be -0.56 and -0.72, respectively. This is in reasonable agreement with α = -0.5 in a prior report by Li *et al*.[1] Theoretical calculations for layered BP predict α = -2 for phonons and α = -0.3 for charged impurity limited scattering.[2,3] Our values suggest that in the metallic regime the mobility is dominated by charged impurity scattering. Furthermore, the values of α decrease as the gate voltage approaches the band edge, suggesting that charged impurity scattering becomes more dominant closer to the band edge. It should be noted that the mobility of our device is ~300 $cm^2V^{-1}s^{-1}$, which is lower than that reported by Li *et al* ~1,000 $cm^2V^{-1}s^{-1}$. The similar values of α measured in both studies, despite the difference in mobility, suggest that charge impurities are an important and possibly intrinsic scattering mechanism in BP devices.

6.4 Variable Range Hopping

For the remaining three gate configurations shown in figure 6.3a, (-4,-4), (-5,-12), and (-6,-20), the device is insulating, i.e. G decreases with decreasing T. Figure 6.3c displays G *vs* T^{-1} in the Arrhenius plot curves; assuming thermal activation ($G \sim exp(-\Delta E_a/k_BT)$) is the main transport mechanism, we obtain activation energies ΔE_a of 71meV, 12meV, and 2meV, respectively. These values are much smaller than those reported for Schottky barriers, which can range from 100 – 700 meV[4,5], depending on the contact

metal, or the band gap (~0.3eV). These unreasonably small activation energies, and the presence of curvature in the Arrhenius plots, prompt us to examine another mechanism that often dominates transport in a disordered system.

As discussed in chapter 2, variable range hopping (VRH) conduction was first described by Mott in 1969 as the probability for conduction electrons to hop between localized states in a disordered medium[6] with a characteristic temperature dependence

$$\sigma = \sigma_0 \exp\left(-\frac{T_0}{T}\right)^p \qquad (1)$$

Here σ_0 is a temperature independent or weekly temperature dependent constant, $p = (1+d)^{-1}$, d is being the dimension of the system, and $T_0 = 13.8/k_b g(\varepsilon) a^2$ with $g(\varepsilon)$ the density of states and a the localization length of the trap states.[7–9] In this 2D system $p = 1/3$, and the 2d density of states $g(\varepsilon) = m^*/\pi\hbar$ where m^* the effective mass of BP. In figure 6.3d we show the semi-log plot of conductivity σ as a function of $T^{-1/3}$. The data falls onto a line for the temperature ranges shown. Fits to the above equation yield T_0 values of 44,000K, 3,600K, and 140K for gate configurations (-4, -4), (-5, -12), and (-6, -20), respectively. From the results in chapter 4, we take $m^* = 0.3m_e$, yielding $g(\varepsilon) = 7.822\times10^{36}\ s^2kg^{-1}m^{-4}$. Thus the localization length is estimated to be a = 1.7 nm, 5.9 nm and 30 nm for each gate configuration. The localization length increases as gate voltages become more negative, which is reasonable, as higher charge concentration provides more screening and reduces the number of trap states.

The origin of these localized states could be either trapped charge impurity states from the BN substrate or intrinsic phosphorus vacancies in the BP lattice. Boron nitride is well known for having low disorder: for instance, the electron-hole puddles in graphene

on BN is reduced by two orders of magnitude than that on SiO_2.[10] Furthermore, recent measurements on pristine BP surfaces demonstrated phosphorus vacancies on lattice surface with distances comparable to the average hopping lengths measured above.[11] In contrast to charged impurity limited mobility in layered samples, the mobilities in bulk BP are dominated by acoustic phonons.[12,13] This change in phonon limited scattering to charge impurity limited scattering between bulk and layered devices, combined with the studies of phosphorus vacancies at the surface, would suggest that phosphorus vacancies play a crucial role in the disorder of mechanically exfoliated BP systems.

In addition to our works, transport via variable range hopping was also observed by other groups. Long *et al* observed T_o ranging from 300 K – 900 K and localization lengths of 10 nm – 20 nm on BN encapsulated devices.[14] Choi *et al* reported T_o between 1000 K – 9000 K on BN encapsulated devices, and observed a coulomb diamond consistent with multiple quantum dots, where the size of the trap state is estimated to be ~25nm.[7] Using BP on SiO_2 and covered with BN, Kuiri *et al* measured localization length of 11 nm.[15] These values are consistent with those reported here and highlight the relatively high concentration of localization states in layered BP.

6.5 Conclusion

In conclusion, we realize p-n-p (n-p-n) and p-p'-p (n-n'-n) electronic phases in a single device by employing a local graphite gate. Variable temperature measurements reveal mobilities limited by charged impurity scattering and localized states around the valence band edge. Comparing the extrapolated localization lengths to phosphorus

vacancies at the surface of BP suggest that the current generation of BP devices still suffers from intrinsic disorder.

References

1. Li, L. *et al.* Black phosphorus field-effect transistors. *Nat. Nanotechnol.* **9,** 372–377 (2014).

2. Liu, Y. & Ruden, P. P. Temperature-dependent anisotropic charge-carrier mobility limited by ionized impurity scattering in thin-layer black phosphorus. *Phys. Rev. B* **95,** 165446 (2017).

3. Trushkov, Y. & Perebeinos, V. Phonon-limited carrier mobility in monolayer black phosphorus. *Phys. Rev. B* **95,** 75436 (2017).

4. Lee, S. Y., Yun, W. S. & Lee, J. D. New Method to Determine the Schottky Barrier in Few-Layer Black Phosphorus Metal Contacts. *ACS Appl. Mater. Interfaces* **9,** 7873–7877 (2017).

5. Ling, Z.-P. *et al.* Black Phosphorus Transistors with Near Band Edge Contact Schottky Barrier. *Sci. Rep.* **5,** 18000 (2015).

6. Mott, N. F. Conduction in non-crystalline materials. *Philos. Mag.* **19,** 835–852 (1969).

7. Choi, S. J. *et al.* Electrical and Thermoelectric Transport by Variable Range Hopping in Thin Black Phosphorus Devices. *Nano Lett.* **16,** 3969–3975 (2016).

8. Kaiser, C. Y. C. and C. G.-N. and L. C. J. and A. B. Conductance of partially disordered graphene: crossover from temperature-dependent to field-dependent variable-range hopping. *J. Phys. Condens. Matter* **25,** 465303 (2013).

9. Ghatak, S., Pal, A. N. & Ghosh, A. Nature of Electronic States in Atomically Thin MoS_2 Field-Effect Transistors. *ACS Nano* **5,** 7707–7712 (2011).

10. Xue, J. *et al.* Scanning tunnelling microscopy and spectroscopy of ultra-flat graphene on hexagonal boron nitride. *Nat Mater* **10,** 282–285 (2011).

11. Kiraly, B., Hauptmann, N., Rudenko, A. N., Katsnelson, M. I. & Khajetoorians, A. A. Probing Single Vacancies in Black Phosphorus at the Atomic Level. *Nano Lett.* acs.nanolett.7b00766 (2017). doi:10.1021/acs.nanolett.7b00766

12. Keyes, R. W. The Electrical Properties of Black Phosphorus. *Phys. Rev.* **92,** 580–584 (1953).

13. Akahama, Y., Endo, S. & Narita, S. Electrical Properties of Black Phosphorus Single Crystals. *Journal of the Physical Society of Japan* **52,** 2148–2155 (1983).

14. Long, G. *et al.* Gate-tunable strong-weak localization transition in few-layer black

phosphorus. (2017). at <http://arxiv.org/abs/1702.04093>

15. Kuiri, M. *et al.* Probing 2D black phosphorus by quantum capacitance measurements. *Nanotechnology* **26,** 485704 (2015).

16. Choi, S. J. *et al.* Electrical and Thermoelectric Transport by Variable Range Hopping in Thin Black Phosphorus Devices. doi:10.1021/acs.nanolett.5b04957

Figure 6.1. a) A micrograph of a the device used in this study. Deep purple structure below device is graphene local gate. b) Conductance G vs V_{inner} at 1.5 K. c) Schematic of local gated structure. An "inner" region is defined by local graphene gate, while "outer" regions are separately controlled by silicon gate.

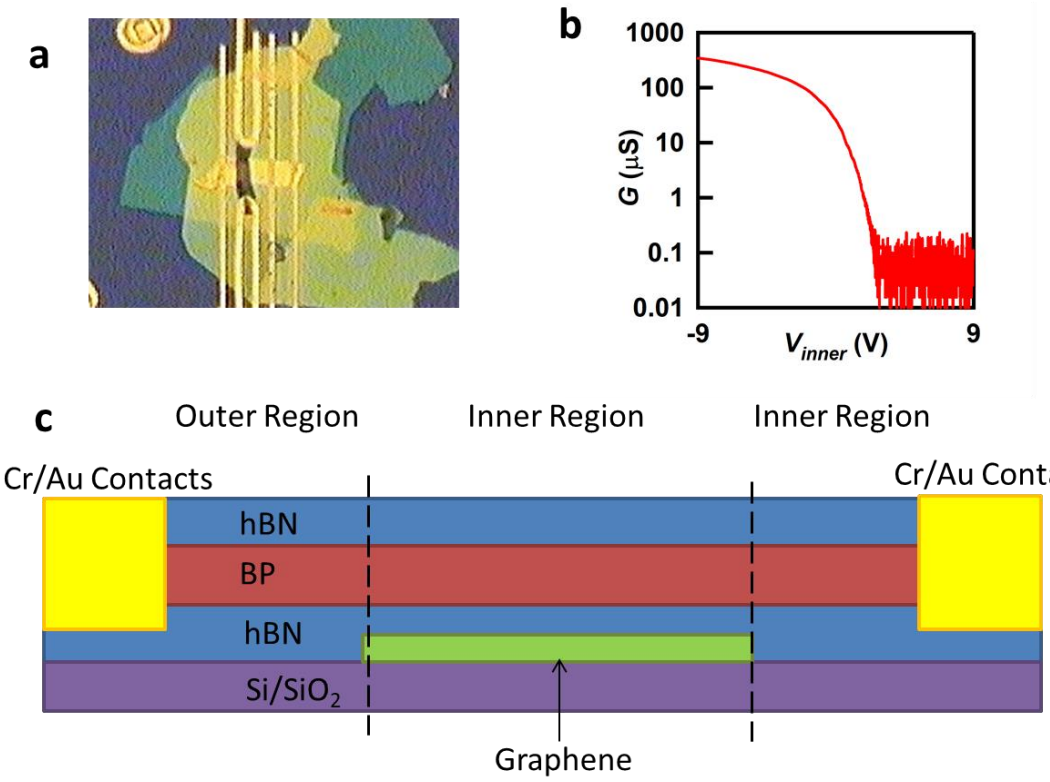

Figure 6.2. a) Conductance G as a function of V_{inner} and V_{outer}. G as a function of V_{inner} at fixed V_{outer} for hole conduction b) and electron conduction c). d) G as a function of V_{outer} at fixed V_{inner} for hole conduction.

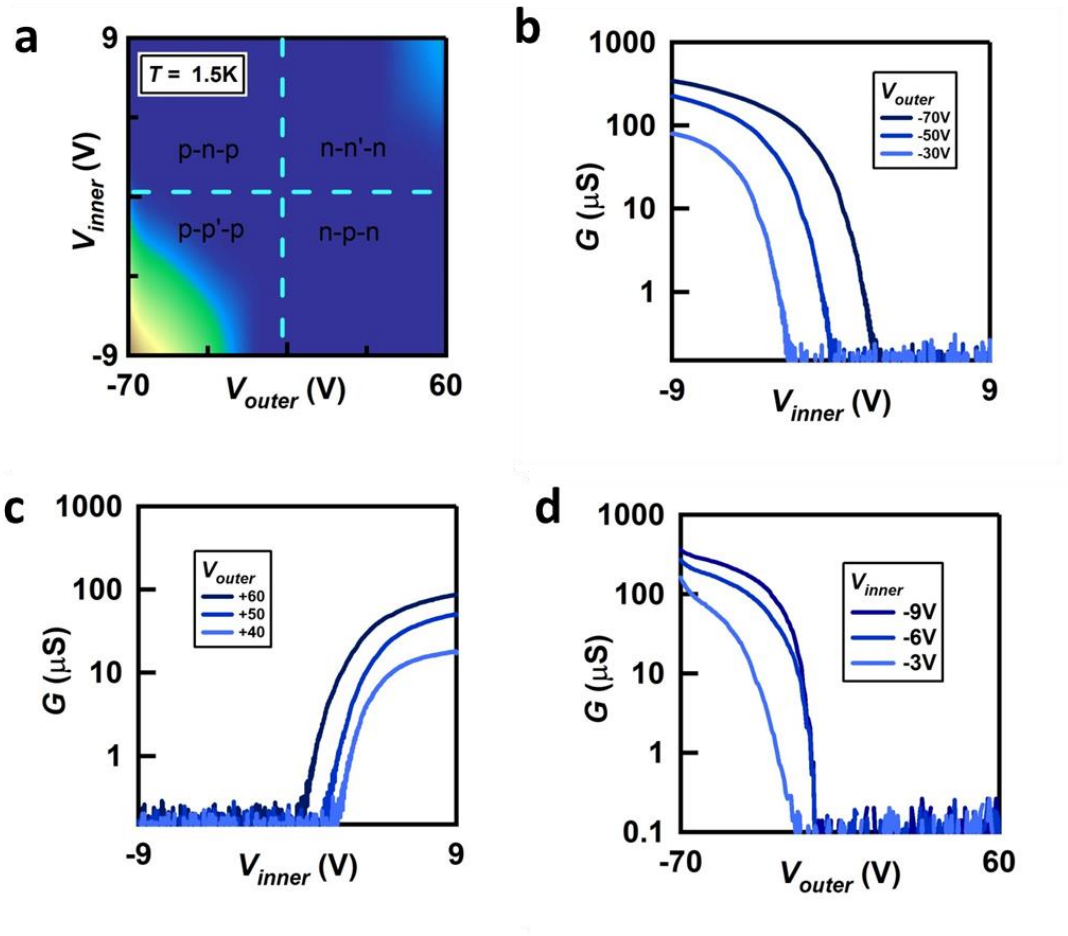

Figure 6.3. a) Conductance G as a function of V_{inner} and V_{outer}. Red dots identify gate configurations (V_{inner} ,V_{outer}) – (-4,-4)V, (-5, -12)V, (-6,-20)V, (-7,-30)V, (-8,-40)V. b) Log-log plot of G as a function of T at gate configurations (-7, -30)V and (-8, -40)V. High temperature fits yield γ values of -0.56 and -0.72 respectively. c) Semi-log Arrhenius plot of conductivity σ as a function of T^{-1} at gate configuration shown. Fits to Arrhenius model give activation energies of 71meV, 12meV, and 2meV, respectively (top to bottom). d) Semi-log plot of σ as a function of $T^{-1/3}$ for gate configurations shown. Fits to variable range hopping model yield T_0 from top to bottom of 140K, 3,600K, and 44,000K.

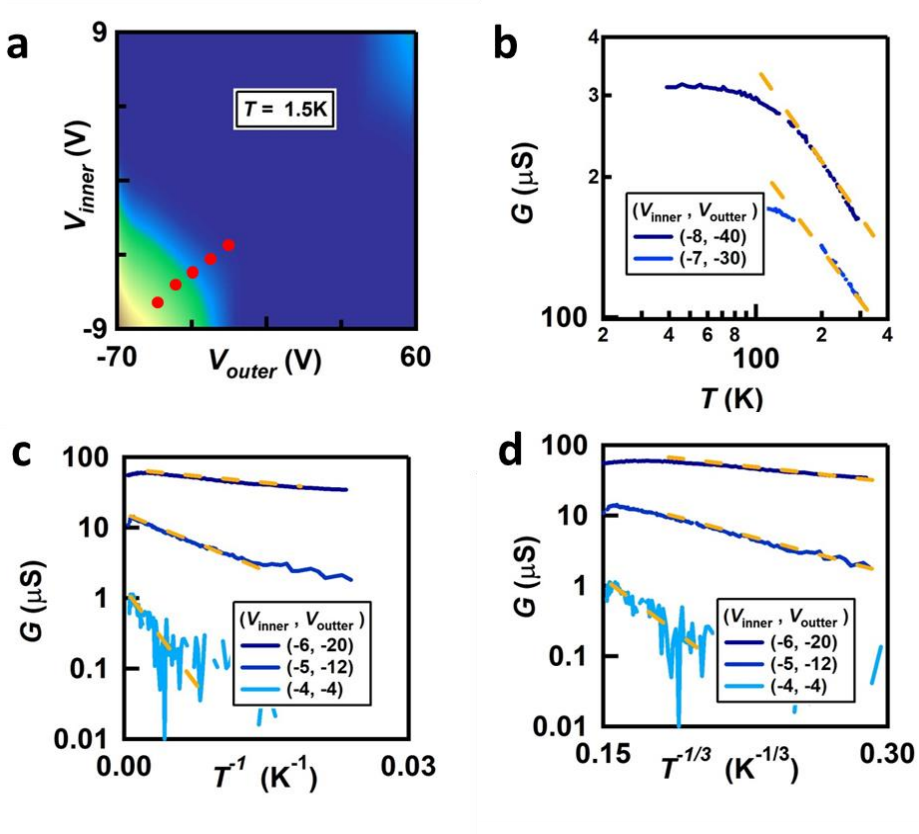

Chapter 7

Conclusion

7.1 Introduction

Since the first generation of layered BP devices, the field of BP electronics and optoelectronics has made tremendous progress. Stability problems[1–3] that plagued device performance were overcome via encapsulation, and the utilization of hBN substrates reduced extrinsic defects and enabled observations of quantum oscillations.[4–7] Gate dependent effective mass and phase relaxation lengths demonstrated the highly tunable properties of BP devices in the metallic regime, and transport mechanism in the semiconducting regime was shown to be dominated by variable range hopping. This period of second generation layered BP devices saw a highly active effort by many groups. In this chapter we will review the accomplishments of this research, highlight the contemporary efforts which paralleled this work, and finally reflect on the future of layered BP device.

7.2 Electrical Properties

As discussed in chapter 4, 5, and 6, several efforts paralleled our own in uncovering the electrical properties of BP. Quantum oscillations were observed by several other groups in encapsulated and un-encapsulated devices on both BN and SiO_2 substrates.[6,8–10] At the time, our observations yielded the highest mobility with oscillations observed as low as 3T, while the closest competitor observe them at 6T. Phase relaxation lengths and their temperature dependence, similar to our own work, were observed by several efforts[11–13], with one group observing a quasi-one dimensional

temperature behavior possibly caused by defects from polymer encapsulation[12]. Localization was observed in the semiconducting regime by a few groups and was well-described by 2D Mott variable range hopping conduction.[13,14]

One of the most exciting achievements to date was the observation of the quantum Hall Effect[15] and field effect mobility in excess of 20,000 $cm^2V^{-1}s^{-1}$.[15–17] These measurements provided insight into the spin dynamics of BP devices demonstrating enhanced *g*-factors, and landau level crossings in a tilted magnetic field. Some open questions remain as to the fractional quantum hall states of BP and how they might differ in an anisotropic medium.

7.3 Thermal and Optoelectronic Properties

Due to the sizeable direct band gap, which can range from 0.3 eV in bulk to 2eV in monolayer, BP is a highly attractive candidate for tunable photodetection in the visible to infrared spectrums. Studies demonstrated fast (1ms) photoresponse[18] and polarization sensitive broadband (400 nm – 3750 nm) photodetection[19]. BP saturable absorbers were demonstrated in several studies and used to generate ~ 3-800 fs short pulses from 1500 – 1900 nm[20], to construct broadband optical modulators from 600 – 2000 nm[21], and to generate energetic short pulses via Q-switching operation from 1000 – 2700 nm[21,22].

Furthermore, measurements on the emission spectra show anisotropic excitonic effects, and substrate dependent emission energies.[23] Polarized Raman studies on the edges of BP reveal the presence of bulk-forbidden modes which depend on the crystal direction and caused by lattice termination rearrangements.[24] Pressure dependent Raman experiments demonstrate a minimum in around 1.1 GPa and are associated with

anomalies in the electron-phonon coupling at the semiconductor topological insulator transistion.[25]

BP is also an appealing material for thermolelectric applications, with theoretical predictions of large energy conversion efficiencies even at room temperature.[26] Large anisotropic thermal conductivities in thin and nano-ribbon samples illuminate the electron-phonon interactions, with suppression of acoustic phonons in thin samples[27] and anisotropic phonon dispersion in nanoribbons[28]. Anisotropies observed in thermoelectric measurements are of the same order observed in electrical measurements ~ 2-3.[27–29]

7.4 Conclusion and Outlook

Studies of properties and applications of atomically thin BP is one of the most active fields of materials research. While many properties of layered BP have been revealed, many more remain to be investigated.

We begin by comparing the revealed properties of layered BP with those of the bulk. In bulk samples the mobility scales with $T^{-1.5}$ which is consistent with phonon limited transport.[30,31] On the other hand the mobility of layered devices, both high quality and disordered, show a $T^{-0.5}$ trend that is consistent with charged impurity limited scattering.[32] The mechanism underlying this change from phonon limited to charge impurity limited scattering remains an open question. Measurements of the anisotropic effective mass[33] on bulk show values which differ than those measured on layered devices[34,35]. Furthermore anisotropic conductivities in bulk[31] remain much larger than those measured in layered samples. These differences would suggest layered devices are

more disordered than bulk. Studies into these differences could reveal a means to achieve higher quality devices.

Interesting properties in bulk, such as superconductivity and crystallographic transitions remain unobserved in layered samples. As discussed in chapter 1, BP undergoes two crystallographic changes under pressure at 5 GPa and 10 GPa with an electronic transition occurring around 2 GPa.[36–38] A recent experiment in bulk BP revealed this transition to suppress the band gap and coincide with a colossal magnetoresistance; a non-trivial berry phase is also observed.[39] Angle-resolved photoemission experiments observed a similar transition in chemically doped BP samples[41] and theoretical calculations[42,43] predict a closing of the gap with applied electric field of 0.5 V/Å. These promising results indicate the possibility of a topological transition under applied pressure or electric field, which could coincide with the development of a Dirac spectrum[40] in the single layer case. This would be the only 2D material, other than graphene, where such a spectrum could be observed. The one missing element from these experiments is a gate to selectively control the density. Density modulated measurements near these pressures and fields where topological transitions occur would illuminate the nature of topological transitions in BP devices.

References

1. Island, J. O., Steele, G. A., Zant, H. S. J. van der & Castellanos-Gomez, A. Environmental instability of few-layer black phosphorus. *2D Mater.* **2,** 11002 (2015).

2. Favron, A. *et al.* Photooxidation and quantum confinement effects in exfoliated black phosphorus. *Nat Mater* **14,** 826–832 (2015).

3. Castellanos-Gomez, A. *et al.* Isolation and characterization of few-layer black phosphorus. *2D Mater.* **1,** 25001 (2014).

4. Tayari, V. *et al.* Two-dimensional magnetotransport in a black phosphorus naked quantum well. *Nat. Commun.* **6,** 7702 (2015).

5. Chen, X. *et al.* High-quality sandwiched black phosphorus heterostructure and its quantum oscillations. *Nat. Commun.* **6,** 7315 (2015).

6. Li, L. *et al.* Quantum oscillations in a two-dimensional electron gas in black phosphorus thin films. *Nat. Nanotechnol.* **10,** 608–13 (2015).

7. Gillgren, N. *et al.* Gate tunable quantum oscillations in air-stable and high mobility few-layer phosphorene heterostructures. *2D Mater.* **2,** 11001 (2014).

8. Cao, Y. *et al.* Quality Heterostructures from Two-Dimensional Crystals Unstable in Air by Their Assembly in Inert Atmosphere. *Nano Lett.* **15,** 4914–4921 (2015).

9. Tayari, V. *et al.* Two-dimensional magnetotransport in a black phosphorus naked quantum well. *Nat. Commun.* **6,** 7702 (2015).

10. Chen, X. *et al.* High-quality sandwiched black phosphorus heterostructure and its quantum oscillations. *Nat. Commun.* **6,** 7315 (2015).

11. Du, Y., Neal, A. T., Zhou, H. & Ye, P. D. Weak Localization in Few-Layer Black Phosphorus. (2016). at <http://arxiv.org/abs/1602.03608>

12. Hemsworth, N. *et al.* Dephasing in strongly anisotropic black phosphorus. *Phys. Rev. B* **94,** 245404 (2016).

13. Long, G. *et al.* Gate-tunable strong-weak localization transition in few-layer black phosphorus. (2017). at <http://arxiv.org/abs/1702.04093>

14. Choi, S. J. *et al.* Electrical and Thermoelectric Transport by Variable Range Hopping in Thin Black Phosphorus Devices. *Nano Lett.* **16,** 3969–3975 (2016).

15. Li, L. *et al.* Quantum Hall Effect in Black Phosphorus Two-dimensional Electron Gas. (2015). at <http://arxiv.org/abs/1504.07155>

16. Long, G. *et al.* Achieving Ultrahigh Carrier Mobility in Two-Dimensional Hole Gas of Black Phosphorus. *Nano Lett.* **16,** 7768–7773 (2016).

17. Tran, S. *et al.* Surface Transport and Quantum Hall Effect in Ambipolar Black Phosphorus Double Quantum Wells. (2017). at <http://arxiv.org/abs/1703.04911>

18. Buscema, M. *et al.* Fast and Broadband Photoresponse of Few-Layer Black Phosphorus Field-Effect Transistors. *Nano Lett.* **14,** 3347–3352 (2014).

19. Yuan, H. *et al.* Polarization-sensitive broadband photodetector using a black phosphorus vertical p–n junction. *Nat Nano* **10,** 707–713 (2015).

20. Sotor, J., Sobon, G., Macherzynski, W., Paletko, P. & Abramski, K. M. Black phosphorus saturable absorber for ultrashort pulse generation. *Appl. Phys. Lett.* **107,** 51108 (2015).

21. Qin, Z. *et al.* Black phosphorus as saturable absorber for the Q-switched Er:ZBLAN fiber laser at 28 μm. *Opt. Express* **23,** 24713 (2015).

22. Kong, L. *et al.* Black phosphorus as broadband saturable absorber for pulsed lasers from 1 *?* m to 2.7 *?* m wavelength. *Laser Phys. Lett.* **13,** 45801 (2016).

23. Surrente, A. *et al.* Excitons in atomically thin black phosphorus. *Phys. Rev. B* **93,** 121405 (2016).

24. Ribeiro, H. B. *et al.* Edge phonons in black phosphorus. **7,** 12191 (2016).

25. Gupta, S. N. *et al.* Raman anomalies as signatures of pressure induced electronic topological and structural transitions in black phosphorus: Experiments and Theory. (2016). at <http://arxiv.org/abs/1612.06135>

26. Fei, R. *et al.* Enhanced Thermoelectric Efficiency via Orthogonal Electrical and Thermal Conductances in Phosphorene. *Nano Lett.* **14,** 6393–6399 (2014).

27. Luo, Z. *et al.* Anisotropic in-plane thermal conductivity observed in few-layer black phosphorus. **6,** 8572 (2015).

28. Lee, S. *et al.* Anisotropic in-plane thermal conductivity of black phosphorus nanoribbons at temperatures higher than 100 K. **6,** 8573 (2015).

29. Jang, H., Wood, J. D., Ryder, C. R., Hersam, M. C. & Cahill, D. G. Anisotropic Thermal Conductivity of Exfoliated Black Phosphorus. *Adv. Mater.* **27,** 8017–8022 (2015).

30. Keyes, R. W. The Electrical Properties of Black Phosphorus. *Phys. Rev.* **92,** 580–584 (1953).

31. Akahama, Y., Endo, S. & Narita, S. Electrical Properties of Black Phosphorus Single Crystals. *Journal of the Physical Society of Japan* **52,** 2148–2155 (1983).

32. Li, L. *et al.* Black phosphorus field-effect transistors. *Nat. Nanotechnol.* **9,** 372–377 (2014).

33. Taniguchi, M. *et al.* Core-level reflectance spectroscopy of black phosphorus single crystals. *Phys. Rev. B* **28,** 1165–1167 (1983).

34. Mishchenko, A. *et al.* Nonlocal Response and Anamorphosis: The Case of Few-Layer Black Phosphorus. *Nano Lett.* **15,** 6991–6995 (2015).

35. Liu, H., Du, Y., Deng, Y. & Ye, P. D. Semiconducting black phosphorus: synthesis, transport properties and electronic applications. *Chem. Soc. Rev.* **44,** 2732–43 (2015).

36. Okajima, M., Endo, S., Akahama, Y. & Narita, S. Electrical Investigation of Phase Transition in Black Phosphorus under High Pressure. *Jpn. J. Appl. Phys.* **23,** 15–19 (1984).

37. Jamieson, J. C. Crystal Structures Adopted by Black Phosphorus at High Pressures. *Science (80-.).* **139,** (1963).

38. Kawamura, H., Shirotani, I. & Tachikawa, K. Anomalous superconductivity in black phosphorus under high pressures. *Solid State Commun.* **49,** 879–881 (1984).

39. Xiang, Z. J. *et al.* Pressure-Induced Electronic Transition in Black Phosphorus. *Phys. Rev. Lett.* **115,** 186403 (2015).

40. Fei, R., Tran, V. & Yang, L. Topologically protected Dirac cones in compressed bulk black phosphorus. *Phys. Rev. B* **91,** 195319 (2015).

41. Kim, J. *et al.* Observation of tunable band gap and anisotropic Dirac semimetal state in black phosphorus. *Science (80-.).* **349,** 723 LP-726 (2015).

42. Fukuoka, S., Taen, T. & Osada, T. Electronic Structure and the Properties of Phosphorene and Few-Layer Black Phosphorus. *J. Phys. Soc. Japan* **84,** 121004 (2015).

43. Liu, Q., Zhang, X., Abdalla, L. B., Fazzio, A. & Zunger, A. Switching a normal insulator into a topological insulator via electric field with application to phosphorene. *Nano Lett.* **15,** 1222–8 (2015).